

Single-Molecule Fluorescence Imaging

Instrumentation Design and Development

Adriel Arsenault

Masters of Physics

Department of Physics

McGill University

Montreal, Quebec

2015-04-15

A Thesis submitted to the Faculty of Graduate Studies in partial fulfillment of the requirements for the degree of Masters of Science

©Adriel Arsenault, 2015

ACKNOWLEDGEMENTS

All of the projects presented in this thesis are the product of a concerted effort between the members of the Leslie Lab. I would like to thank Dan Berard who has always taken time to give me his technical advice. Jason Leith and Chris McFaul, who had both joined previous to my arrival, trained me and continued to be available for advise throughout my program and whose contributed much of the material of the papers that we published to the Review of Scientific Instruments [1, 2]. Shane Scott and Gil Henkin are both members who I worked with, and often sought their expertise on microscopy and bio-related issues. I would also like to thank the members of the Leslie Lab who have all aided me in indirect ways, such as Alec Silver, Alex Hoffkircher and Jill Lauren whose work in the bio-lab I benefit from. I am also grateful to the μ Manager software and development team as well as Andrew Caleb Guthrie, Alexander Verge, and Yang Zhou for their help to our particular implementation of the software. I would like to thank François Michaud for his work on the COMSOL simulations (section 2.3), and for his unique artistic sense with which he curated the more aesthetically pleasing of the figures presented here. I would also like to thank Pascal Bourseguin and Steve Kacani for their role in machining many of the custom pieces presented in these devices. I would also like to thank Matthew Tarling, whose original work on the home-built microscope I adopted, and Richard Talbot who I worked in close colaboration with on this project. I would also like to thank the agencies who have contributed funding for this project: the Natural Sciences and Engineering Research Council of Canada NSERC, the Canada Foundation

for Innovation (CFI), the Department of Physics, McGill University and the Cellular Dynamics of Macromolecular Complexes Program (CDMC) for the graduate fellowship that they awarded me, Jackie Vogel, and Christian Baron who I learned much from as part of the the CDMC program. Finally, special thanks to Sabrina Leslie who helped and guided me throughout this research.

ABSTRACT

My masters research has been devoted to the design, development, and characterization of new instrumentation hardware for the Leslie biophysics lab. The first instruments I present in this thesis are variations of devices used for Convex Lens-induced Confinement (CLiC) imaging. These CLiC devices improve background rejection and extend diffusion-limited observation times. A powerful feature of CLiC imaging technology is the ability to examine single molecules under a continuum of applied confinement, from the nanometer to the micrometer scale. I demonstrate the basic functionality of the CLiC device by confining freely diffusing λ -phage DNA and show a manipulation of their molecular conformations and diffusivity, showing that these devices are well suited to tackling open problems in biophysics, biotechnology, nanotechnology, materials science, and chemistry. Secondly, I present the design and construction of a versatile, open-frame inverted microscope system for widefield fluorescence and single-molecule imaging. The microscope chassis and modular design allow for customization, expansion, and experimental flexibility. I demonstrate the Microscope's functionality through experiments utilizing the two-color imaging system that provides the option of imaging multiple molecular species simultaneously. Together, the flexibility of the open-framed chassis endowed with these features allows for a wide range of applications.

ABRÉGÉ

L'objectif principal de ma recherche de maîtrise a été la conception, le développement et l'installation de nouvel équipement d'instrumentation pour le laboratoire de biophysique Leslie Lab. Les premiers instruments présentés dans cette thèse sont des variantes de dispositifs utilisés pour l'imagerie par confinement induit par lentille convexe (Convex Lens-induced Confinement ou CLiC). Ces dispositifs CLiC améliorent l'élimination du bruit de fond et prolongent le temps d'observation limité par la diffusion. Une caractéristique puissante de l'imagerie par CLiC est sa capacité à observer individuellement des molécules sous un continuum de confinement, du nanomètre au micromètre. Je démontre les fonctions de base du dispositif CLiC en confinant des molécules d'ADN de λ -phage en diffusion libre et j'effectue une manipulation de leur conformations moléculaires ainsi que de leur diffusivité, démontrant que ces dispositifs conviennent à l'étude de problèmes ouverts en biophysique, en biotechnologie, en nanotechnologie, en sciences des matériaux et en chimie. En second lieu, je présente la conception et la construction d'un système de microscopie à fluorescence inversé polyvalent et à châssis ouvert pour l'imagerie unimoléculaire à large champ. La conception modulaire du châssis laisse place à la personnalisation, l'expansion et à la flexibilité expérimentale. Je démontre les fonctionnalités du microscope en effectuant des expériences utilisant le système d'imagerie bicolore permettant d'observer différentes espèces moléculaires simultanément. Ensemble, la flexibilité du châssis ouvert doté de ces fonctionnalités permet un large éventail d'applications.

TABLE OF CONTENTS

ACKNOWLEDGEMENTS	ii
ABSTRACT	iv
ABRÉGÉ	v
LIST OF TABLES	viii
LIST OF FIGURES	ix
1 A Brief Introduction to Optical Microscopy	1
1.1 History and Scientific Background	1
1.2 A Brief Review of the Fundamentals of Optical Microscopy in Biophysics	3
1.2.1 Image Formation and Magnification	3
1.2.2 Resolution	5
1.2.3 Contrast	8
1.2.4 Principles of Fluorescence Microscopy	9
1.3 CLiC Microscopy	13
1.3.1 Motivation for CLiC Microscopy	13
1.3.2 Working Principle of CLiC Microscopy	15
2 CLiC Device Development	19
2.0.3 Motivation and Overview	19
2.1 Manual CLiC Device	20
2.2 Piezo-Controlled CLiC Device Development	22
2.2.1 CLiC 2.0	23
2.2.2 MadCity CLiC	27
2.3 Implementation of Flow-Cells	34
2.4 Performance and Applications	42
2.4.1 CLiC Chamber Formation	42
2.4.2 Particle Tracking	44

3	Home-Built Fluorescence Microscope (HBM)	48
3.1	Introduction and Motivation for the Home-Built Microscope . . .	48
3.2	Custom Microscope	50
3.3	Excitation Optics	52
3.4	Dual-Channel Imaging System	54
3.5	Performance and Applications	58
	3.5.1 Single-Molecule Photo Bleaching	58
	3.5.2 FRET With Dual-Channel Imaging	60
4	Conclusions and Future Directions	64
	4.0.3 Conclusions	64
	4.0.4 Future Directions	65
	REFERENCES	69

LIST OF TABLES

<u>Table</u>		<u>page</u>
2-1	Circular flow-cell data for different film thicknesses.	39
2-2	Finite element analysis data for rectangular flow-cells of different h_{PDMS} thicknesses.	40
3-1	Custom Components of Chassis	52
3-2	List of Optical Components Shown in Figure 3-2	56

LIST OF FIGURES

<u>Figure</u>	<u>page</u>
1-1 Object and image location shown with a ray diagram for a thin lens	3
1-2 Demonstration of an infinity corrected microscope emission pathway, and the composition of an objective lens	6
1-3 Demonstration of the Rayleigh criterion for optical resolution	7
1-4 Schematic of the excitation and emission of a standard inverted fluorescence microscope	10
1-5 Working principle of CLiC microscopy	17
2-1 3D model of the manual flow-cell CLiC device	21
2-2 Schematic of the CLiC 2.0 device with magnified inset of the rotation piece.	23
2-3 Interactive 3D drawing showing a cross-section of the Z-axis mechanics of the CLiC 2.0 device	25
2-4 Interactive 3D drawing of the CLiC 2.0 device	26
2-5 Interactive 3D figure of the improved “MadCity” CLiC device.	29
2-6 Cross section of the MadCity CLiC fluidics delivery system	33
2-7 Model of flow-cell compression used in finite element analysis	37
2-8 Schematic of the coverslip-coverslip contact point along the designated minor axis for the simulated circular chamber flow-cell.	38
2-9 Method of chamber characterization utilizing the dual-channel imag- ing system	42
2-10 Diffusion coefficients and in-plane radius of gyration of λ -phage DNA molecules.	44

3-1	Schematic of the microscope chassis.	50
3-2	Excitation and dual-emission optical pathways	54
3-3	Single molecules photobleaching taken with the home-built microscope using TIRF.	59
3-4	FRET assay using bound oligonucleotides labeled with Cy5 and complementary oligo labeled with Cy3	63
4-1	Evolution of the home-built microscope	67
4-2	Further planned modifications to the home-built microscope	68

CHAPTER 1

A Brief Introduction to Optical Microscopy

1.1 History and Scientific Background

The focus of my research has been the design, development, and characterization of new microscopy hardware for the Leslie biophysics lab. These instruments I have developed consist of a number of devices used for Convex Lens-induced Confinement (CLiC), and an inverted fluorescence microscope with dual-channel imaging capabilities. Much of this work has previously been published, and the material in Chapter 2 is the main content of a paper currently being prepared for publication [1, 2, 3]. In this thesis additional details are given, and the instrumentation is presented in a chronological order which provides a clearer history of the development of the devices.

This work on optical and fluorescence microscopy instrumentation contributes to a field with over four centuries of history and continuous development. The optical microscope is currently one of the most widely used scientific research tools and plays a prominent role in most biological and biophysical research. The first examples of instrumentation that used a system of lenses to magnify visible light may have been created as early as the late 1590s [4]. By the mid to late 1600s the field of biology had been revolutionized by this instrument. The Royal Societies publication of Robert Hooke's *Micrographia*, which contained detailed reproductions of drawings of his observations, helped popularize the importance and power of the new instrument, as

well as first introduced the concept of the cell. Along with Robert Hooke, Antonie van Leeuwenhoek was another early pioneer in the field of microscopy whose discoveries of bacteria and protists, spermatozoa, cellular vacuoles and muscle fibers earned him the common distinction of “the Father of Microbiology ” [5].

Since the microscope’s early inception and initial ground breaking discoveries it has continued to be widely used and extremely influential. Microscopy hardware and techniques have continued to evolve and increase the realm of possible applications. Innovations in optical microscopy are ongoing and of continuing importance as shown by the 2014 Nobel Prize in Chemistry awarded to Eric Betzig, William Moerner and Stefan Hell for “the development of super-resolved fluorescence microscopy,” which brings “optical microscopy into the nanodimension ” [6].

1.2 A Brief Review of the Fundamentals of Optical Microscopy in Biophysics

A brief review of the basic concepts of optical microscopy is provided below. This introductory section may be of particular use to a future student of the lab who may be continuing with some aspect of these projects. Briefly, In order for microscopists to observe objects smaller than the eye can see, a microscope must provide the three following conditions: magnification, resolution, and contrast. An image can only be useful for scientific analysis if the objects being examined are significantly magnified with details of interest which are well resolved and distinguishable from the background.

1.2.1 Image Formation and Magnification

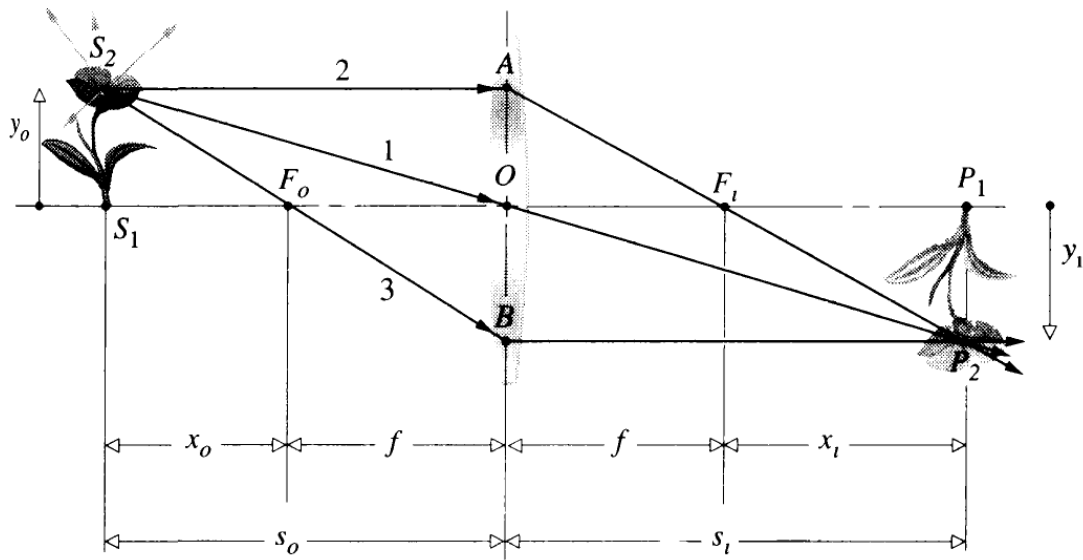


Figure 1-1: Object and image location shown with a ray diagram for a thin lens. Image reproduced from Hecht's Optics, page 163 [7].

Figure 1–1 demonstrates the ray-diagram for the creation and position of an image by a simple thin lens. The (transverse) magnification M_T of an image is a ratio that relates the size of the image to the size of the actual object being imaged through an optical system. That is,

$$M_T \equiv \frac{y_1}{y_o} \quad (1.1)$$

or as can be deduced from basic trigonometry:

$$M_T = -\frac{s_1}{s_o} \quad (1.2)$$

For an object located with $f > x_o > 0$ a real inverted magnified image is formed on the opposite side of the lens. In order to calculate the magnification using the ray tracing method within an optical system consisting of multiple lenses, the image of the n th lens is used as the object of $n + 1$ th lens in the series of lenses.

In an infinity corrected compound microscope the magnification is produced by at most three lenses: the objective, the tube lens and the ocular lens. Briefly, the objective is the lens closest to the object which gathers light from the sample, the tube lens is designed to focus the light from an objective onto a detector (or ocular), and the ocular (or eyepiece) is the lens that focuses the light into an image on the retina of the eye. Microscope objectives consist of a complicated (and costly) systems of lenses, as can be seen from Fig. 1–2 b). These lenses work together to optimize image quality by reducing optical aberrations in ways a single simple lens cannot. However, for simplicity we depict the objective as a single lens which has the

characteristics of the entire system of lenses. The magnification of the microscope is the product of the magnification power of the objective and the ocular lens.

Most modern microscopes have an infinity corrected imaging system as depicted in Fig. 1–2 a). An infinity corrected optical system is one in which the image distance of the objective is set to infinity. Instead of having a fixed tube length distance (previously 160mm was the accepted standard set by the Royal Microscope Society), infinity corrected systems have no fixed distance to the detector, and rather use a tube lens to focus the final image. This is the basic format for the home-built microscope which is depicted in Section 3, except for the fact that the image is formed directly on the camera chip without the need for an ocular lens.

1.2.2 Resolution

While magnification is a necessary function of a microscope it is not alone a sufficient condition for creating useful images; the details of interest within the image must also be clearly resolved. For objects to be resolved they must be identifiable as separate objects. This condition is stated more formally by the Rayleigh criterion:

Two point sources are regarded as just resolved when the principal diffraction maximum of one image coincides with the first minimum of the other.

If the distance is greater, the two points are well resolved and if it is smaller, they are regarded as not resolved [9].

To understand what this means in terms of a microscope system, it is important to first understand the concept of the point–spread function (PSF). The point–spread function for an optical system is simply the image that is produced by imaging a point like object. For a single ideal spherical lens, a point source creates a PSF in

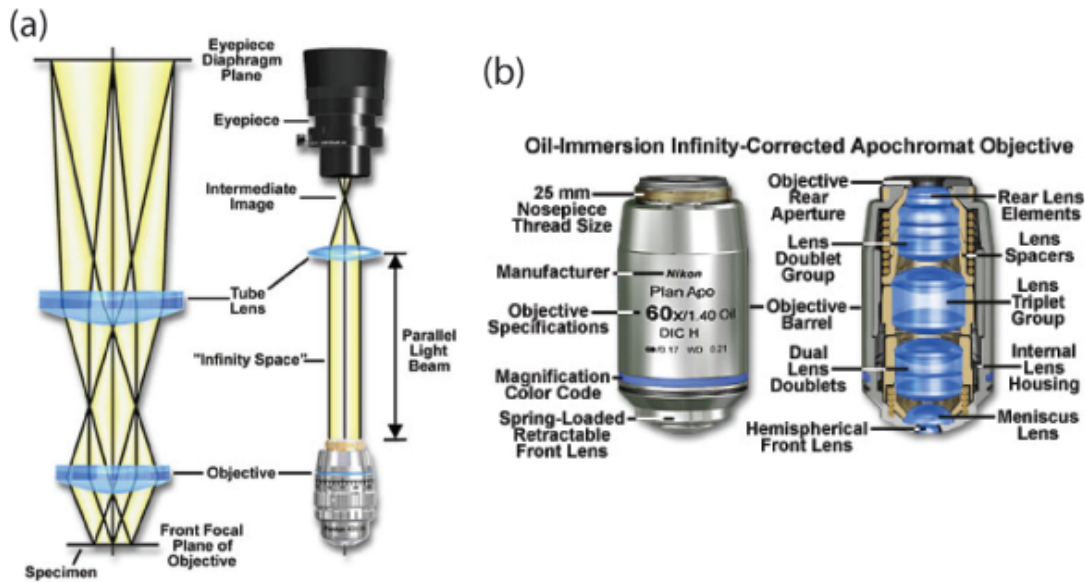


Figure 1-2: Demonstrates an infinity corrected microscope emission pathway, and the composition of an objective lens. a) an infinity-corrected microscope system. The left hand side of a) shows the focal points at the front focal plane of the objective. The right side of a) more clearly demonstrates the infinity-space (the space in which the light is collimated) between objective and tube lens. b) shows a schematic of the lens system within a typical objective lens. Image taken from Olympus Microscopy Resource Center [8].

the image plane (X-Y plane) defined by an Airy disk. The airy disk is shown in fig. 1-3 (a) (above) which appears as a central spot, or intensity peak, with diffraction rings of maxima and minima surrounding it; the intensity profile is plotted below demonstrating that the majority of the intensity is contained within the central peak (the zeroth order maxima). Figure 1-3 (b) demonstrates two Airy disks which are minimally resolved according to the Rayleigh criterion, and Fig. 1-3 (c) demonstrates two Airy disks which are not resolved.

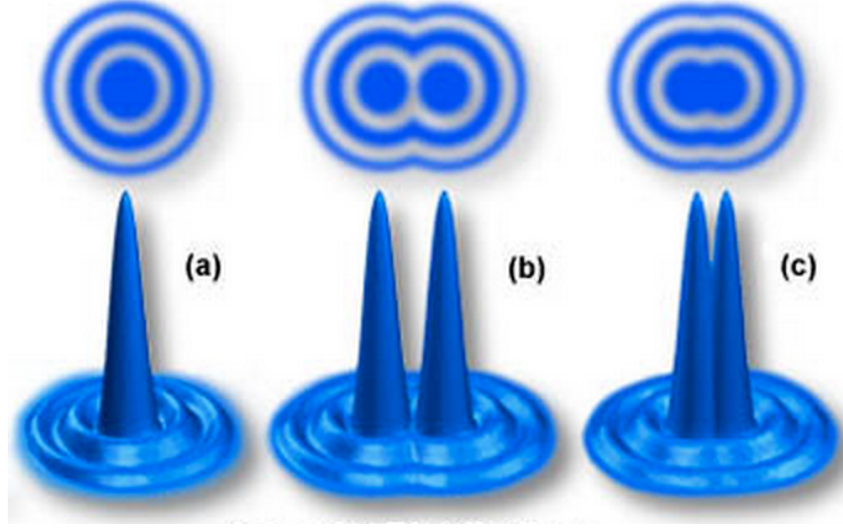


Figure 1-3: Demonstration of the Rayleigh criterion for optical resolution. (a) represents an Airy disk in the (X-Y) plane Below (a), (b), (c): surface plots of the intensity profiles are shown. (b) demonstrates two Airy disks which are minimally resolved according to the Rayleigh criterion, while (c) demonstrates a case where two objects are not resolved. Image from Olympus Microscopy Resource Center [10].

The resolution of a microscope is therefore the shortest distance by which two point-like objects can be separated and still be identifiable as separate objects according to the Rayleigh criterion. This distance corresponds to the diameter d of the central spot of the airy disk which depends on the wavelength, λ , of the light being imaged, the index of refraction n , and the half-angle of light gathered from the sample θ . The Abbe diffraction limit states:

$$d = \frac{\lambda}{2n\sin(\theta)} \tag{1.3}$$

The term $n\sin(\theta)$ is often called the numerical aperture (denoted by NA). For all experiments throughout this thesis an objective with an NA of 1.4 was used.

This means that a microscope imaging emitted light with wavelengths between 500 nm-700 nm would have diffraction-limited spot-size of ~ 200 nm-250 nm.

Recently various microscopy techniques, collectively termed “super-resolution” have been created which improve resolution beyond the Abbe diffraction limit [11]. These techniques achieve this by various means; techniques such as near-field scanning optical microscopy (NSOM), and stimulated emission depletion microscopy (STED) attempt to find physical means to beat the traditional diffraction limit. NSOM places a detector very close to the sample (less than the wavelength of light) to capture evanescent waves, while STED uses two lasers simultaneously to selectively deactivate a region of excited fluorophores (see Section 1.2.4) allowing for a much smaller excitation spot and thereby improving resolution [12, 13]. Techniques such as stochastic optical reconstruction microscopy (STORM), and photo-activated localization microscopy (PALM) primarily achieve diffraction-limited images through image analysis [14, 15]. Individual particles within multiframe stacks are fit to Gaussians, and thereby located with sub pixel accuracy. While each technique has its own particular limitations, together these techniques expand the range of resolvable samples for optical investigation.

1.2.3 Contrast

Even an object which has been imaged with sufficient magnification and properly resolved can only be viewed clearly if it is distinguishable from the image background. In order to achieve this with translucent objects, biologists often stain their samples. This often achieves the desired effect, however it has many limitations. Foremost, it requires that the sample is biologically inactive and immobilized. Additionally

certain stains and samples can cause artifacts leading to the false appearance of biological-structures [7].

Other methods have arisen which use new microscope hardware to achieve greater contrast rather than altering the sample. Differential interference contrast (DIC) separates light by polarization creating two images separated laterally by the resolution distance of the microscope. When the two separate images are recombined into the final image, the optical path difference between the two images creates regions of interference, and therefore greater contrast [16]. Phase contrast is a similar technique that transforms phase variations which are invisible to the human eye into variations in brightness [17].

1.2.4 Principles of Fluorescence Microscopy

A relatively new type of optical microscopy has emerged which utilizes fluorescent molecules allowing for much greater resolution and contrast in many applications. Fluorescence microscopy creates an image using only the light emanating from fluorescent molecules within the sample which greatly increases the signal to background ratio for images. This is possible due to the Stokes shift of the fluorescent molecules: the offset between the absorption spectrum and the lower energy emission spectrum. By using a dichroic with an appropriate transmission profile (ideally approaching a Heaviside function with a half maximum somewhere between the absorption and emission peaks) the microscope is able to excite with one wavelength and image in others. A schematic of how this is achieved is demonstrated in Fig. 1-4.

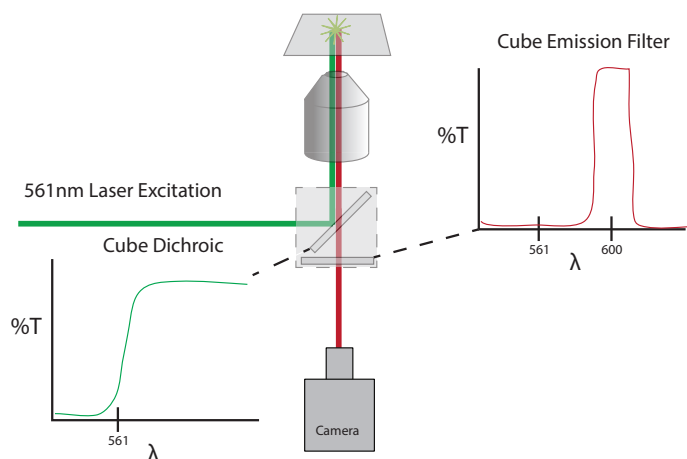


Figure 1–4: In this example the sample is excited by laser light with a wavelength of 561 nm. The excitation light meets a dichroic mirror on a 45 degree angle with a transmission (T) profile which strongly reflects at 561 nm. This light is focused by the objective and excites the fluorescent molecules within the sample. The excitation light is then prevented from reflecting back to the camera by the same dichroic mirror. Light emitted by the fluorophores is then captured by the objective and directed towards the camera. The emission filter typically only transmits a band of wavelengths that is chosen to be centered on the optimal section of the fluorophore emission profile, and which reflects any unwanted light from excitation and background.

In this example, laser light with a wavelength of 561 nm excites the sample. The excitation light meets a dichroic mirror on a 45 degree angle with a transmission (T) profile which strongly reflects at 561 nm. This light is focused by the objective and excites the fluorescent molecules within the sample. The excitation light is then prevented from reflecting back to the camera by the same dichroic mirror. Light emitted by the fluorophores is then captured by the objective and directed towards the camera. The emission filter typically only transmits a certain band of wavelengths chosen to be centered on the optimal section of the fluorophore emission profile, and which reflects any unwanted light from excitation and background sources.

Along with general widefield fluorescence imaging, new single-molecule microscopy techniques have emerged in line with the development of fluorophores, including confocal, and total internal reflection (TIRF). Confocal Microscopy was developed in order to increase resolution and contrast by using a system of pinholes to exclude light rays emanating from objects within other focal planes [18, 19]. TIRF microscopy uses evanescent waves to excite a thin layer of the sample, typically ~ 20 nm, which allows only those molecules bound to a surface to fluoresce. The resulting image has higher contrast due to less background emissions from non-bound molecules [20].

Fluorescence microscopy techniques have opened up the possibilities of single-molecule studies to be done with optical microscopes. While a molecule of interest, such as a typical protein, may be more than 2 orders of magnitude smaller than the diffraction limit, it is still possible to observe the way in which these molecules behave and function by examining light emanating from a reporter fluorophore which is bound to it. These approaches allow information normally hidden within statistical ensembles – such as an individual molecule’s structure, position, or state – to be probed directly. Single-molecule experiments based on fluorescence microscopy have led to critical discoveries spanning the fields of physics, [21, 22] chemistry, [23, 24] biology, [25, 26, 27, 28] and materials science [29, 30]. In the field of biophysics, for example, single-molecule microscopy has uniquely identified and characterized transient components of a number of biological pathways [25, 26, 27, 28].

Since its introduction, fluorescence microscopy has served as a workhorse for molecular and cell biology. A wide range of synthetic fluorescent dyes have been developed and optimized, and many fluorescent proteins that are expressed directly

within host cells have been isolated and modified [31]. The ample number of options means that nearly any biomolecular target can be labeled and observed using a fluorescence microscope. This success of fluorescence microscopy techniques, as indicated by the 2014 Nobel Prize in chemistry alone, has ensured that they will remain valuable tools for researchers, and continue to furnish new discoveries.

1.3 CLiC Microscopy

1.3.1 Motivation for CLiC Microscopy

A large section of my graduate work has been devoted to a particular fluorescence microscopy technique called Convex Lens Induced Confinement (CLiC). This technique was first conceived of by my supervisor Dr. Sabrina Leslie in order to address certain limitations existing within the field of fluorescence microscopy [32]. As previously mentioned, two commonly used single-molecule techniques are confocal and TIRF microscopy. While these techniques are used in a vast array of laboratories to understand important biological systems, they nevertheless face several challenges when probing systems with weak or cooperative molecular interactions and slow dynamics [32]. This is especially true when at least one molecular species is required to be at micromolar or higher concentrations. For example, single-molecule resolution is limited to reagent concentrations less than 10 nM for confocal, and 100 nM for TIRF microscopy, corresponding to one molecule per detection volume [32].

Time available for detection is also an important consideration. For example, imagine the case of a freely diffusing protein. The StokesEinstein equation gives an equation for the diffusion coefficient of a spherical particle:

$$D = \frac{K_b T}{6\pi\eta r} \quad (1.4)$$

Where K_b is the Boltzman constant, T is the temperature in Kelvin, η is the dynamic viscosity of the fluid, and r is the radius. The average radius of a folded protein is $r \approx 2 \text{ nm}$. Using a temperature of 300 K, and a dynamic viscosity of water of $\eta = 1000 \text{ Pa s}$, the Stokes-Einstein equation gives a diffusion coefficient of

$D \sim 100 \mu\text{m}^2\text{s}^{-1}$. This means that the average protein will exit the detection volume of the microscope in hundreds of microseconds to milliseconds, for TIRF and confocal microscopy respectively [32]. These constraints on accessible reagent concentrations and observation times limit the capacity of these approaches in probing the slow dynamics or weak, cooperative, and transient interactions which characterize many physiological processes of interest [32].

A compelling challenge for modern fluorescence microscopy is visualizing the trajectories of protein molecules undergoing extended molecular searches on topologically complex DNA under physiological conditions [33, 34]. It has been theorized that a DNA repair protein’s search for a lesion in the genome can be accelerated by “facilitated diffusion” which involves alternating rounds of one-dimensional and three-dimensional diffusion. Experimental investigation of these processes is challenging for a number of reasons: 1.) the time for molecules to associate with one another can range from seconds to minutes; 2.) a wide field of view is necessary to visualize the extended search; 3.) the background fluorescence due to physiological concentrations of freely-diffusing proteins can obscure single proteins from view; and 4.) DNA topology is an important variable in these theories but is highly complex in physiological systems. The physiological significance of results obtained using confocal and TIRF microscopy can be limited by their observation conditions: TIRF microscopy is typically performed using low protein concentrations and DNA which is immobilized to the surface under applied flow [33]. While these conditions facilitate observations of molecular trajectories, they restrict the DNA topology and reagent conditions, with a number of possible consequences.

Overcoming the simultaneous challenges of observing concentrated solutions for long time-periods is relevant not only to making advances in biophysics, but also to addressing open questions in soft-matter physics, chemistry, and nanoscience. For instance, to elucidate the microscopic rules governing the self-assembly of materials and the emergent phenomenon of active matter [35], it is essential to perform new kinds of measurements of the interactions and dynamics of individual components (e.g. microtubules, actin monomers and filaments) in free-solution, posing a challenge to current technologies. CLiC imaging addresses these issues and allows for imaging freely diffusing DNA and other biopolymers with improved signal to noise under physiological conditions.

1.3.2 Working Principle of CLiC Microscopy

CLiC imaging is based on a simple principle: to confine molecules to a thin chamber, which is formed by bringing a top curved surface into contact with a bottom planar surface. There are two modes of operation for standard CLiC. The first does not use a flow-cell; the confinement is created when an optical “push lens” makes contact with a coverslip [32]. For this reason this method has been termed “lens-coverslip CLiC.” Two distinguishing features of this approach are: 1.) using pre-characterized curved chamber-surfaces and 2.) allowing the top and bottom chamber-surfaces to be translated with respect to one another.

More commonly CLiC is used in combination with a Flow-Cell. For this method the CLiC imaging chamber is created when the “CLiC lens,” or “push-lens” presses into the top coverslip, causing it to deform. This process is demonstrated in fig. 1–5. The top surface curves downward until it comes into contact with the bottom planar

coverslip surface at a single point. The optical-grade, fused silica surfaces (ESCO Products) ensure minimal auto-fluorescence and provide ~ 2 nm surface separation at contact due to the inherent surface roughness (verified using Atomic Force Microscopy) [32]. The chamber height, which is defined as the separation between the confining (top and bottom coverslip) surfaces, increases very gradually away from this contact point, e.g., by ~ 10 nm over a ~ 100 μm field of view. The deformation and chamber shape has been rigorously characterized through both simulation and experiment (results shown in Section 2.3).

The use of flow-cells offers several advantages compared to the original lens-coverslip implementation: reproducible and temporally-controlled sample insertion, no evaporation, no exposure of the sample to ambient gases, complete sample exchange between serial measurements, compatibility with lithography or chemical functionalization of the confining surfaces, reduced sample volume (~ 6 μL per chamber) and a sample chamber which is potentially composed of common and disposable parts (e.g. glass coverslips). The push-lens does not make direct contact with the sample; therefore rigorous laborious cleaning protocols between measurements can be relaxed. Finally, and importantly, this implementation aims to facilitate incorporation of the CLiC technique into a wide array of experiments. Flow-cells are a staple of single-molecule microscopy and biology laboratories; thus existing surface-treatment and sample preparation steps need not be altered when implementing CLiC imaging hardware.

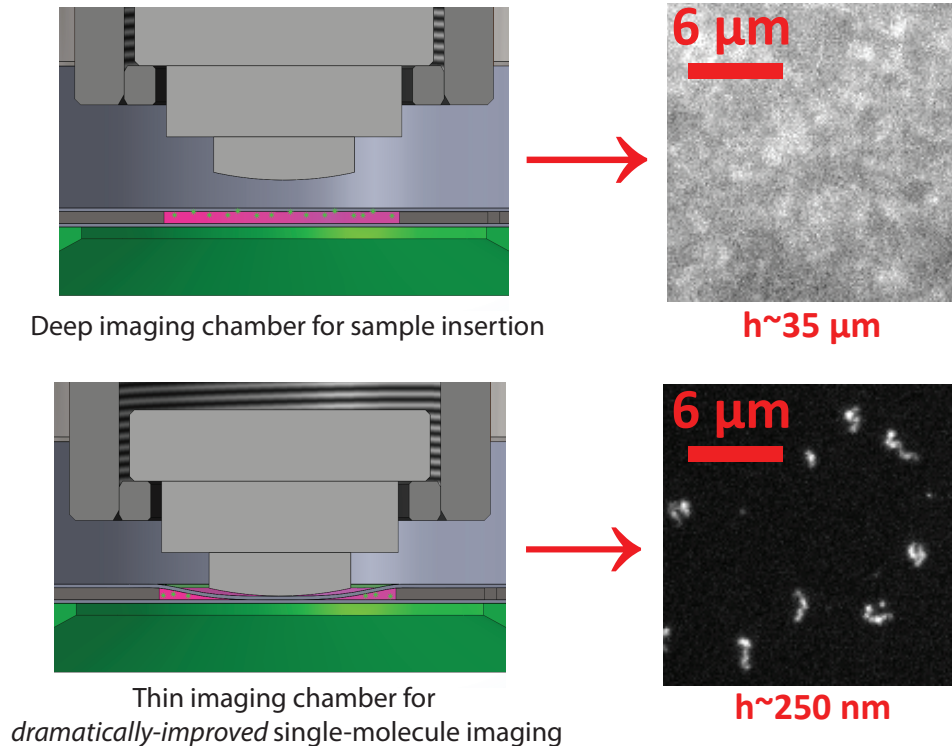


Figure 1–5: Working principle of CliC microscopy. Molecules are initially confined between two glass coverslips separated by $30 \mu\text{m}$ thick double-sided tape while the push-lens is raised (top). The lens then presses down onto the top coverslip, causing it to deform. The top surface bows downward until it comes into contact with the bottom coverslip surface at a single point (bottom), forming the chamber geometry. Molecules are confined to within a single focal plane which greatly increases image quality.

With either method, the act of confining molecules within a thin chamber reduces the detection volume and thus allows samples with higher reagent concentrations to be used for single-molecule studies. The small detection volume offers the dual advantages of suppressing background fluorescence and extending the observation times of freely diffusing molecules. For instance, the trajectories of small proteins

confined within the focal plane can be tracked for tens of seconds within a $100 \times 100 \mu\text{m}^2$ field of view. CLiC has previously been used to extend single-molecule imaging to micromolar reagent concentrations using chamber heights as small as $\sim 5 \text{ nm}$ [32]. When recently applied to the procession of myosin motor proteins on actin filaments, CLiC has achieved at least five-fold-enhanced background-rejection in comparison to TIRF imaging (using sufficiently tall chambers so as not to influence physiological procession rates on substrates tens-of-nanometers thick) [36].

The further advantage of CLiC microscopy is the potential to capture, probe, and influence the configurations of single molecules. CLiC's graduated confinement profile (which typically varies by tens of nanometers in height over hundreds of micrometers) allows for the microscopy of molecular dynamics and interactions as a function of applied confinement. Further, the size-dependent exclusion of molecules from a graduated chamber facilitates imaging a wide range of molecular topologies, and provides a quick approach to measuring the relative size distribution of small molecules [32].

A powerful example of such molecular manipulation has been demonstrated in a recent publication of a new application of CLiC [37]. Nanoscale features etched into surfaces were combined with the dynamic and precise control of the vertical confinement gradient provided by CLiC in order to achieve new measurements. This technique was shown to be successful in loading DNA into nanochannels which is a potential breakthrough for DNA sequencing methods. This technique could be extended to loading, lysing, and processing genomic material from single-cells [37].

CHAPTER 2 CLiC Device Development

2.0.3 Motivation and Overview

The first major focus of this work has been the design and development of CLiC devices which enable the CLiC technique. In this section I present three modular CLiC instruments which are able to convert an ordinary inverted fluorescence microscope into a precise single-molecule spectroscopy station suitable for various experiments within the fields of biology, biophysics, chemistry, materials science, and medicine.

The three devices presented in this section all stem from the original CLiC instrument which was created by Sabrina Leslie during her post-doctoral research [32]. Prior to my arrival in the Leslie lab, Daniel Berard redesigned the original manual device into the first piezo-driven model for his bachelor thesis work. My work on instrumentation followed from this point where I developed CLiC 2.0 and the subsequent version: the “MadCity-CLiC” which derives its name from the custom designed stepper-motor stage designed in collaboration with Mad City Labs. While we in the Leslie lab now perform experiments which nearly exclusively require the more precise nano-positioner versions (sections 2.2.1 and 2.2.2), we have reworked the original manual device as a complimentary module for the home-built microscope (HBM) (Section 3). In the remaining sections of this chapter I will expand on the design considerations and motivations for each of these devices.

2.1 Manual CLiC Device

The earliest manual CLiC imaging devices emphasized ease of implementation by using catalogue-accessible components and simple, custom-machined parts [32, 36]. These hand-operated and low-budget instruments succeed in improving single-molecule imaging and performing various types of confinement experiments. While our lab’s particular needs have outstripped the capabilities of these simple devices, we nevertheless recognize the utility that their simplicity may offer to other researchers who wish to utilize the CLiC technique without a prohibitive price-tag.

In order to make this research tool available for others we have redesigned the manual device and published it as a modular add-on to the home-built microscope (Section 3) [2]. Together these instruments constitute a versatile and cheap home-built single-molecule imaging station. While the manual device is capable of working with any inverted microscope, we find that the manual device and the HBM are similar in their “do-it-yourself” character and therefore well suited to be published together; the manual CLiC device would likely suit the needs and price range of those who may be interested in building their own fluorescence microscope.

Figure 2–1 demonstrates the manual CLiC device that we have included with our home-built microscope to form a single-molecule microscopy station [2]. The device operates as follows: The CLiC device rests atop a sample plate that is bolted to the microscope stage. Custom aluminum fittings hold a steel shaft that acts as a rotation-axis for an extended lever arm. On this lever, the push-lens is fixed in a recess by means of setscrews. The lever is initially raised to allow for sample insertion and lowered by adjusting a nut on a finely threaded rod at the opposite end

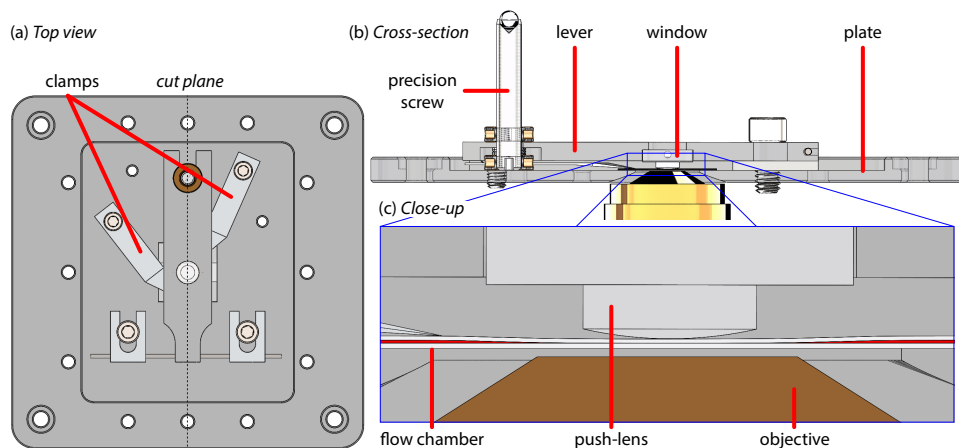


Figure 2-1: 3D model of the manual flow-cell CLiC device. (a) Top view of the device. The four largest holes are for fastening the plate onto the microscope. The clamps can be positioned on either set of holes in the central part of the plate depending on the flow-cell size. (b) Cross-section of the CLiC device. The lever can be displaced by turning the lock-nut, which rotates on a 1/4-100”-threaded screw. (c) Close-up of the cross-section at the contact point between the flow-cell and the push-lens. The thickness of the tape was exaggerated (to 100 μm) to show the deformation of the top coverslip. The displayed top and bottom coverslips are respectively 145 μm and 175 μm thick. The oil objective is typically positioned 170 μm away from the bottom of the bottom coverslip.

of the lever. As the nut is tightened towards the plate, the lens presses down on the flow-cell, which is held over the imaging aperture by custom spring clips. A spring applies a restoring force that ensures gradual chamber compression and removes the backlash in the adjustment nut.

The simple design also allows for easier customization of experiments. While this device lacks the extreme precision of the computer controlled device (presented in Section 2). It is able to take data that is of comparable quality to other CLiC devices.

2.2 Piezo-Controlled CLiC Device Development

While the hand-operated and low-budget CLiC instruments do succeed in improving single-molecule imaging, they nevertheless have certain drawbacks. For instance, the CLiC lens can only be lowered with a precision of ~ 0.5 microns and had no encoders for position readout. Further, the fine threading of the lock-nut means that adjustment of the CLiC lens takes a long time to adjust correctly, which limits the number of experiments performed in a given time-frame. This may be a hindrance when using samples which have limited lifetimes of bio-activity. Meeting the experimental needs of our laboratory has necessitated our move away from manual devices towards nanopositioner driven devices which we have optimized for precise, highly reproducible and high-throughput measurements of multiple samples.

Here I present the conception, fabrication, and demonstration of two versatile, computer-controlled piezoelectric CLiC devices which transform a standard inverted fluorescence microscope into a precision single-molecule imaging station. Like the manual devices, these versions of CLiC employ a tunable imaging chamber to enhance background rejection and extend diffusion-limited observation periods. Using nanopositioning stages along side optical encoders, this device achieves repeatable and dynamic control over the tunable geometry of the sample chamber on scales as small as the size of individual molecules, enabling regulation of their configurations and dynamics. Unlike the manual devices, these devices also utilize microfluidics for serial sample insertion as well as sample recovery, facilitating temporally controlled, high-throughput measurements of multiple reagents.

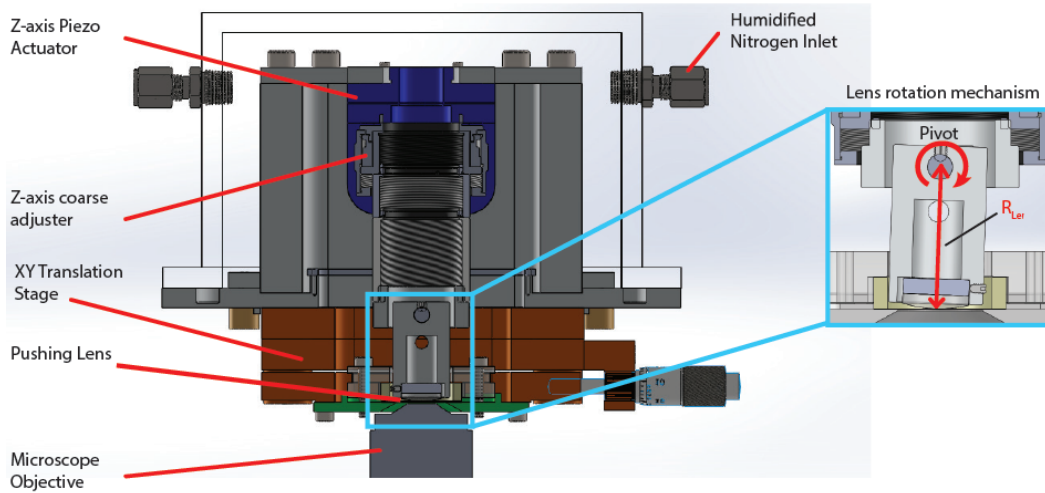


Figure 2-2: Schematic of the CLiC 2.0 device with magnified inset of the rotation piece.

2.2.1 CLiC 2.0

The first CLiC device that I designed followed from the original piezo-driven CLiC device created by Daniel Berard for his bachelor thesis work (referred to as CLiC 1.0). This device first successfully employed a piezoelectric controlled tunable geometry for optical microscopy, nevertheless this device had a number of issues which needed to be corrected, namely in terms of accessibility and ease of use. The design of CLiC 2.0 is shown by Figs. 2-2, 2-3, and 2-4, the last two of which are interactive 3D models embedded in the PDF document.

The driving force of the push-lens is generated by a P-725 PI-Foc (Physik Instrumente) piezoelectric Z-actuator which has $250 \mu\text{m}$ of travel. This actuator has 0.3 nm resolution over this range, delivering sensitivity for nanoscale spectroscopy. The piezo-actuator is supported by custom housing depicted in Fig. 2-3 and accepts

a lockable lens tube (Thorlabs SM1ZM, 4mm length-adjustment) to hold the push-lens (e.g. Thorlabs LA4966, LA4765, or LA4600). The flow-cell chamber is centered with respect to the push-lens using a micrometer-driven XY stage (MadCity Labs, custom-design, with 2 mm of travel and $\sim 0.1 \mu\text{m}$ resolution). This ensures that the resulting chamber geometry is symmetric. Additionally, this stage can be used to align features on the coverslip surface with respect to the push-lens. For alignment applications that require nanometer precision, an XY piezo nano-positioning stage (P-733, 100 μm travel) can be exchanged for the micrometer-stage which was deliberately designed with the same dimensions.

This device was created during a phase of our lab’s history when a predominant amount of experiments were performed using the “lens-coverslip” method (as described in Section 1.3.2). Due to this method, the sample is exposed to ambient conditions. To help prevent evaporation and reduce damage of the sample (such as photo-bleaching which is enhanced by oxygen in solution), the entire device was designed to be sealed by an air-tight Plexiglas box, into which humidified nitrogen is pumped prior to sample insertion using the inlets and outlets in Fig. 2–4. In the implementation of CLiC 1.0, the aluminum housing itself was designed to create an airtight seal. In practice this limited accessibility to the sample and hindered the progress of experiments

At the time when we were performing lens-coverslip experiments, we found that the push lens would often become contaminated with adhered molecules from the sample. Once this occurred we would then need pause the experiment and elaborately clean the push lens according to our piranha protocol (described in Section 2.3). To

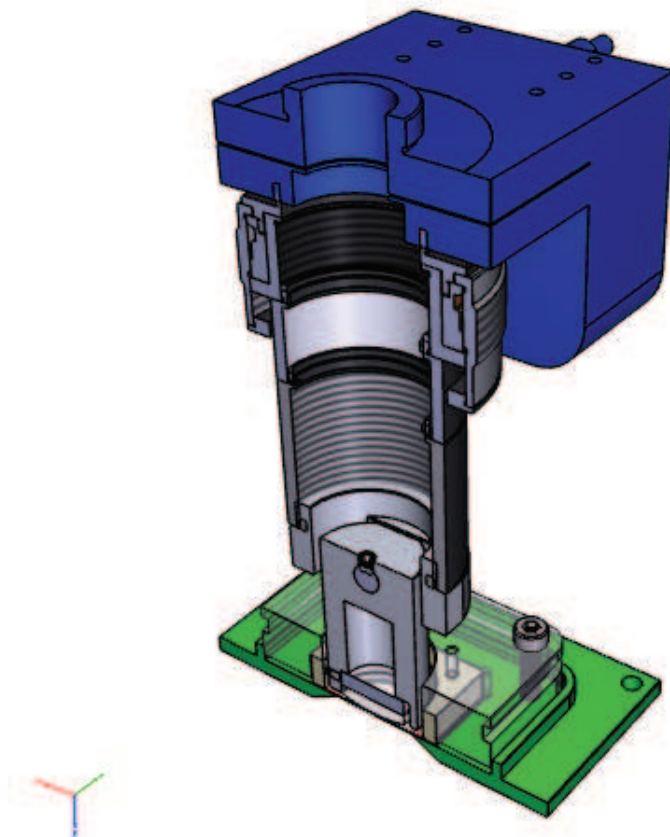


Figure 2–3: Interactive 3D drawing showing a cross-section of the Z-axis mechanics and sample holder of the CLiC 2.0 device, including the rotation piece. To activate the 3D model, click on the image while viewing the document within a viewer with Acrobat-9/X compatibility. Use ctrl to pan and shift to zoom.

circumvent this problem CLiC 2.0 was designed to be compatible with a push-lens “rotation-piece” for the push lens that was designed by Dan Berard. By rotating the CLiC lens (as depicted in Fig. 2–2) it is possible to use different contact locations on the lens surface for independent experiments. For convenience and, a rotation-pivot

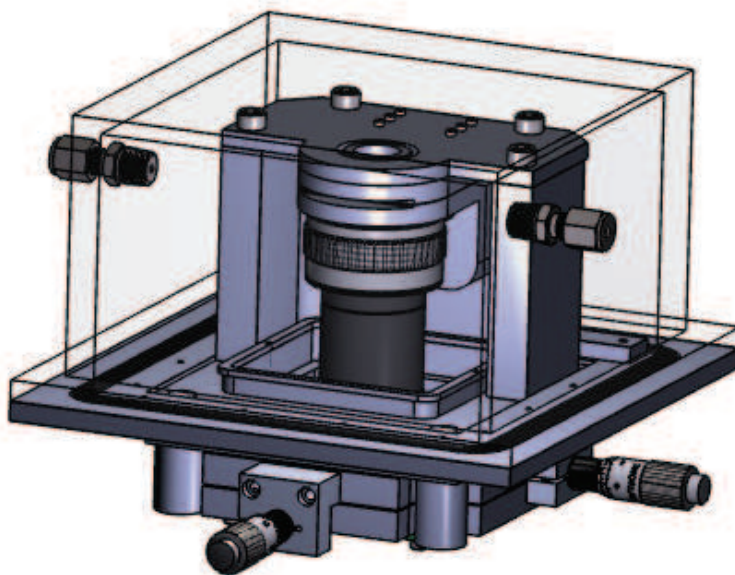


Figure 2–4: Interactive 3D drawing of the CLiC 2.0 device. To activate the 3D model, click on the image while viewing the document within a viewer with Acrobat-9/X compatibility. Use ctrl to pan and shift to zoom.

is positioned a distance above the lens surface approximately equal to the lens' radius of curvature; thus, the XY location of the contact point on the bottom coverslip does not change significantly when the lens is re-lowered into contact.

CLiC 2.0 Fluidics System

The ability to programmatically insert and recover samples is key to performing high-throughput and temporally resolved measurements of dynamics and interactions. As previously mentioned, CLiC 2.0 boasts an improved and computerized fluidics delivery system in comparison with the manual version. Instead of pipetting the sample directly into the flow-cell, the sample is injected into the flow-cell (prior to lowering the push-lens) using a custom microfluidics system and computer-controlled syringe-pumps (New Era NE-500). Samples are initially loaded into micro syringes (100 μL , Luer-Tip, Cole Parmer RK-07938-23) using blunt stainless steel needles (1/2 in, 30 Gauge Luer Polypropylene Hub, Amazon Supply B0013IZT9K). Chemically inert PTFE tubing (ID 0.01 in, OD 0.0625 in, IDEX Health and Science 1527) connects these outlets to small holes (1/32" diameter) which are sand-blasted into the corners of the top surface of the microscopy chamber. A PDMS gasket (~ 6 mm thick) creates a seal between the tubing and the top surface, and an acrylic block presses downward upon the PDMS gasket to maintain this seal. This fluidics system was further improved upon with the creation of the MadCity CLiC device.

2.2.2 MadCity CLiC

The design for CLiC 2.0 was ultimately shaped by certain design constraints – namely the choice of piezoelectric positioner. The Design required the use of the PI-Foc simply because this was previously purchased for CLiC 1.0. Although the PI-Foc was functional, it was not designed for use in such an application. The manufacturers designed and marketed it for nano-focus of microscope objectives. When

incorporated into our CLiC device, the shape was cumbersome and requires mounting the push lens in a way that creates a large cantilever. Additionally, there is a 1”- diameter hole through the middle of the piezo-actuator that the manufacturers designed in order to accommodate the light path. Unfortunately this served no purpose for our CLiC design except to structurally weaken the device. With the MadCity CLiC many of the design constraints had shifted allowing for greater design flexibility. Additionally, by this time our lab’s experimental focus had moved away from lens-coverslip experiments that required cumbersome methods for sealing humidified nitrogen. In this way it could be designed for accessibility and ease of use, as the sample would be sealed within the flow-cell. Also of significance for the design considerations was the fact that more funds were available for the device and the purchase of more appropriate piezo-actuators.

A schematic of the MadCity CLiC device is shown in Fig. 2–5. The device is supported by a plate (yellow) that bolts to the microscope’s XY stage. On this platform the main brace (light blue) and micro-XY stage (dark grey) are bolted. The brace provides a sturdy vibration resistant support for the Z-actuator assembly. This assembly is made out of two stages: A micro positioner for coarse control (Brown) and a piezo-actuator for nanoscale positioning (Dark Blue, Madcity Nano-OP30). A lens tube clamp (red) is mounted to the piezo-actuator. A groove is cut into the bracket that allows for thumb screws (not shown) to quickly fasten or unfasten the two protruding clamps. On the micro XY stage the sample plate (green) and fluidics assembly are mounted. The fluidics system is shown in greater detail in Fig. 2–6 and is fully explained in the following subsection.

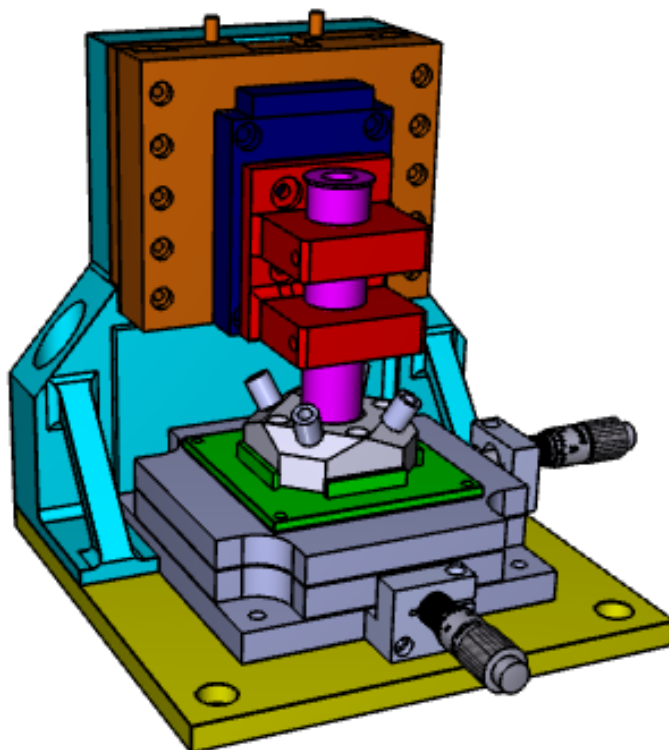


Figure 2-5: Interactive 3D figure of the improved "MadCity" CLiC device. To activate the 3D model, click on the image while viewing the document within a viewer with Acrobat-9/X compatibility. Use ctrl to pan and shift to zoom.

Unlike previous devices which use a single piezo-actuator to position the lens tube, this device uses a combination of micro and nanoscale stages offering two advantages: 1) greater total range of motion of the push-lens 2) the use of a piezo-actuator with specifications more suited to this application as the piezo-actuator no longer needs such an extreme range of travel. The Z actuators in the new device are a custom version of a commercially available stage ensemble (Madcity, Nanospmz) traditionally used for Atomic Force Microscopy (AFM) applications. The micropositioner is a stepper motor stage with dual rows of crossed roller bearings for enhanced stability. The stage has 25 mm of total travel with a minimum step-size of 95 nm and an optical encoder which measures position to 20 nm. Since the micropositioner has a large range of motion, the nanopositioner no longer needs to travel the full distance needed to compress the flow-cell. This allows for the use of a piezo-actuator device with greater precision and stiffness to be selected, as these qualities are often inversely proportional to the total travel range. The new nanopositioner (Mad City, Nano-OP30) has a travel range of 30 μm and has a closed loop positional resolution of 60 picometers. This is compared to 250 μm of travel with a maximum closed loop positional resolution of 0.75 nm for the previous nano positioner (PI-Foc, PI-725) used in CLiC 2.0. The stiffness is also increased from 0.17 $N/\mu\text{m} \pm 20\%$ to 3.0 $N/\mu\text{m} \pm 20\%$ which allows for more force to be applied which may be a factor for certain experiments.

Along with these improvements to precision, the design of the new device offers a more convenient lens tube configuration. The CliC 2.0 device required the lens tube to be directly threaded to the Z-actuator; It could not be changed, cleaned or

adjusted without the piezo-actuator being fully retracted from the sample to allow the tube to clear the chuck, and then fully unthreaded from the device. In the MadCity design the lens tube is held by clamps and therefore can be quickly locked or unlocked by means of two thumb screws. This allows the lens to be quickly removed for easy access to the sample chuck. This feature also allows lens tubes containing lenses of varying radii to be swapped or cleaned within a matter of seconds.

This configuration also allows a much more open system and easy access to the sample. Due to certain design considerations the sample rests on the top of the meso-stage, and not bolted to the bottom as it previously had been with CLiC 2.0. This can be accomplished with the MadCity version for two reasons. The first being that unlike with the PI-Foc, the push-lens can be clamped anywhere along the lens-tube, and not only screwed in by one end of the lens tube. By clamping the lens tube closer to the point of contact with the sample, this reduces the overall height required for the piezo-actuator device and subsequently the length of the cantilever, creating a more stable contact point.

By fastening the sample plate to the bottom of the meso-stage rather than the top, the height of CLiC 2.0 was lowered by ≈ 5 inches. As that device had 4 solid aluminum walls, this meant a substantial saving in terms of weight and cost of materials. The height of the MadCity device is of less concern as the z-stages are only supported from the back.

MadCity Fluidics System

The fluidics delivery system for the MadCity device is another significant improvement from the previous version. The CLiC 2.0 device used a syringe pump and

tubing to insert the sample into the flow-cell. While functional, this system had the disadvantage of occasionally flowing air bubbles into the sample chamber if the lines and syringe were not meticulously purged and secured. Even if operated correctly, the system left a large amount of sample in the dead volume of the fluidics lines ($\sim 100 \mu\text{m}$). This is often a major hindrance if the sample was difficult or expensive to create in large quantities. This current version of the CLiC device has a new fluidics system that successfully addresses these issues.

Instead of flowing the sample through tubing, the newly designed chuck has loading ducts (see Fig. 2–6) into which the sample is directly pipetted. On the top of these ducts there are ferules (Cole Parmer, RK-45501) which make an airtight lock with luer tipped PVC tubes (Cole Parmer, RK-30600). These tubes are connected to air-filled syringes that are controlled by syringe pumps (New Era, NE-500). The syringes no longer directly pump the sample. Instead, compressed air forces the sample into the flow-cell through a hole in the top coverslip. This method has the benefits of allowing for much smaller sample sizes to be used, faster loading times, and fewer parts to clean and install between experiments. Previously, the minimum total sample size per experiment, depending on chamber size and tube length was $\sim 100\mu\text{L}$ - $120\mu\text{L}$, the required minimum sample size with the new system is now $\sim 10\mu\text{L}$ - $20\mu\text{L}$. The faster loading times and ease of cleaning allow for more experiments to be performed within the same time duration, with less risk of sample contamination from difficult to clean parts such as the tubing.

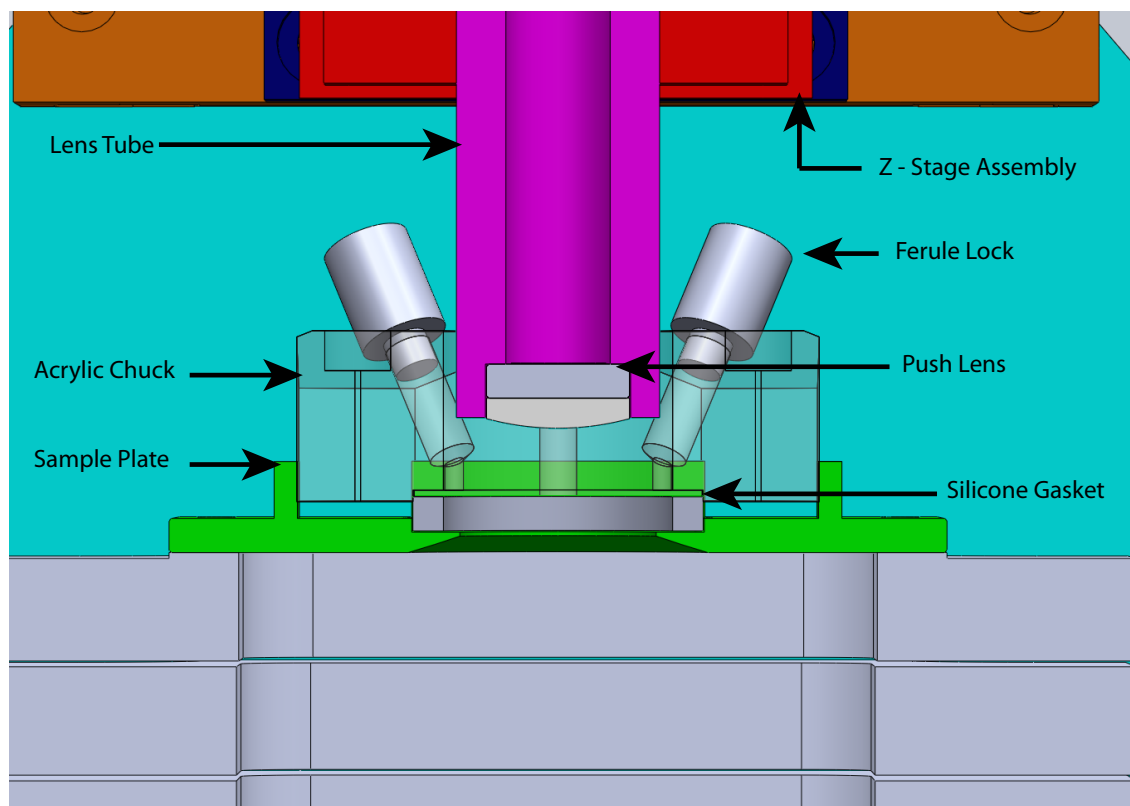


Figure 2–6: Cross section of the MadCity CLiC fluidics delivery system. The CLiC lens is held by the lens tube (magenta) and is driven through the aperture in the acrylic sample chuck. The chuck contains angled loading chambers topped with airtight ferule locks. When compressed air from the syringes is applied, the sample enters the chamber through a hole in the top coverslip that is sealed to the chuck by means of a silicone gasket (McMaster Carr 5787T35).

2.3 Implementation of Flow-Cells

A major part of the development of the CLiC technique was also spent in the creation and characterization of the flow-cells we use. As the geometry of the flow-chamber is crucial for CLiC experiments, considerable time was put into understanding and perfecting the geometry of flow-cells. I began the study of the flow-cell geometry using COMSOL, a simulation package for finite element analysis. My initial studies of the deformation geometry and fluid flow were then carried forward by François Michaud who adapted them for other materials and geometries. The following section is the result of a number of these simulations that first appeared in conference proceeding for the International Society for Optics and Photonics [3]. The following section is a report on the simulation and experimental characterization of this tunable chamber geometry, and its influence upon the diffusion and conformations of DNA molecules over extended observation periods. We have developed a predictive model for the CLiC chamber geometry in order to equip researchers with quantitative measures of key microscopy parameters as a function of readily available instrument components.

Before discussing the results of the simulations a few words should be said about the fabrication of these flow-cells: The flow-cell used in CliC imaging is typically constructed from two coverslips separated by double-sided adhesive (30 μm thick, Nitto Denko No.5603) or a film made from PDMS. The adhesive is laser-etched with flow-channels through which liquid can enter the central imaging chamber (by Peter Shaw, PBS Engraving). The flow-cell sits within a square recess embedded in the

top surface of a custom sample plate, whose bottom surface contains a conical recess designed to accept the objective.

Before construction, the glass coverslips are rigorously cleaned of all contaminants by a multi-step process; glass coverslips in a ceramic cradle were sonicated in HellmanexIII (Hellma Analytics), ethanol, and acetone for 30 minutes each, rinsing thoroughly in deionized water (DIRECTQ 5UV-4, Millipore) after each sonication. Coverslips were then cleaned in piranha solution, with a 2:1 proportion of sulfuric acid to hydrogen peroxide. After sitting for an hour, piranha solution was disposed in an appropriate container. Coverslips were sonicated in water, rinsed in acetone, and then sonicated in acetone. 1.0 mL of APTES was added to 80 mL of acetone in the beaker, the solution was agitated, and allowed to sit for 10 minutes. Coverslips were then rinsed thoroughly and stored in deionized water

Quantitative Simulations of the flow-cell CLiC geometry

Using COMSOL Multiphysics (version 4.3b) we have simulated the CLiC imaging chamber implemented using two kinds of flow-cells: one with a circular channel with inlets (Fig. 2-7 a) and one with an 8-mm wide rectangular channel (Fig. 2-7 b). We have modeled the chamber geometry as a function of accessible parameters, including the film thickness, radius of curvature of the push-lens (R_p), and “over-push” distance, defined as the distance by which the push-lens is translated past coverslip-coverslip contact. This predictive model enables experiment-specific understanding and selection of important chamber parameters such as the size of the in-focus region and radius of curvature of the chamber. Throughout this section, default device parameters are taken as: 30- μm thick film, a 145- μm thick top coverslip (#1 coverslip),

a 175- μm thick bottom coverslip (#1.5 coverslip), a 30-mm focal length push-lens (Thorlabs LA4966), and zero over-push distance. An applied over-push causes the top coverslip to indent the bottom coverslip in a circular region of mean radius of contact r_b , as illustrated by Fig. 2-8.

In the simplest imaging setup, the objective is translated in a single horizontal plane containing the contact point (e.g. without using an auto-focus feedback mechanism). In the final CLiC imaging chamber, the bottom surface of the bottom coverslip curves away from the objective, by an amount equal to δ . Its top surface curves by the same amount, as illustrated by Fig. 2-8b. Molecules appear in-focus when the separation between the plane containing the contact point and top confining surface, $h + \delta$, is less than the focal depth, taken to be 1.5 μm . Tables 2-1 and 2-2 show the size of this in-focus region. The size of this region increases when the tape thickness decreases, and is weakly affected by the over-push distance.

For the circular flow-cell, the flexure of the bottom coverslip towards the objective is effectively negligible for typical operating parameters. The in-focus region is characterized by a diameter of 1506 μm on major axis A and 1477 μm on minor axis B, and maximum chamber height of 1.46 μm on major axis A and 1.45 μm on minor axis B (see Fig. 2-7 c,d). This region can be extended to 1528 μm on major axis A and 1509 μm on minor axis B, corresponding to a chamber height equal to the focal depth, by employing an auto-focus mechanism. Similarly, for the rectangular flow-cell, the in-focus region is characterized by a diameter of 1068 μm on major axis A (988 μm on minor axis B), and a maximum chamber height of 1.33 μm on major

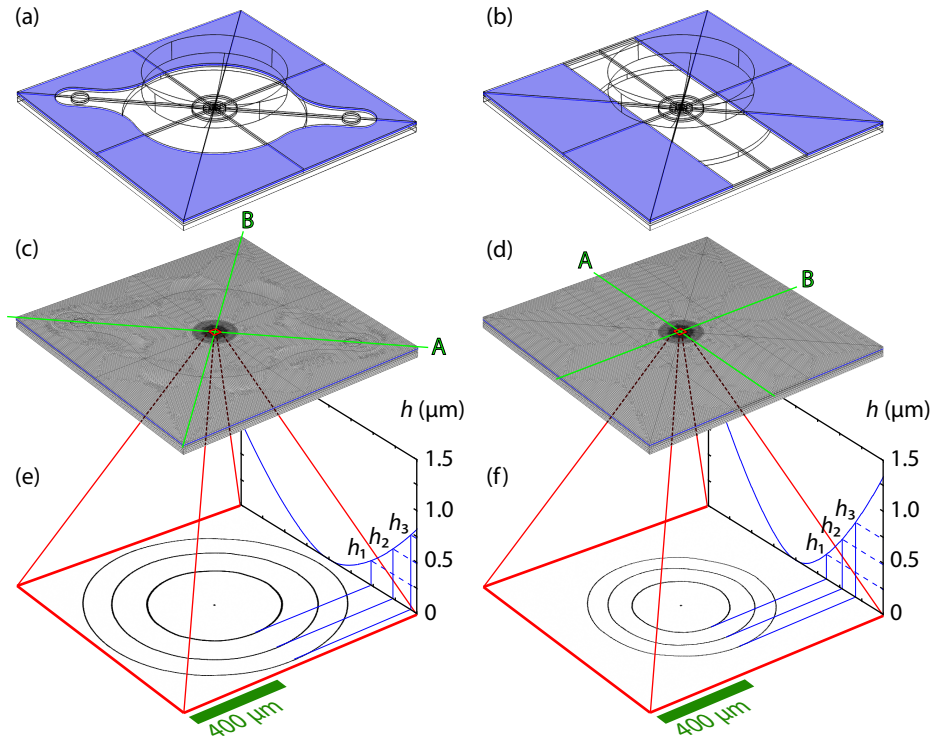


Figure 2-7: Model of flow-cell compression used in finite element analysis. (a, b) Wireframe renderings of the circular and rectangular flow-cells, showing the push-lens above and plate below. The $30\text{-}\mu\text{m}$ thick PDMS film is highlighted in blue. (c) Overview of the mesh used for the circular flow-cell and the plate. The mesh element precision is refined toward the center, where it is $23\ \mu\text{m}$. (d) Similar overview of the mesh used for the rectangular flow-cell and the plate, with minimum mesh element size at the center of $20\ \mu\text{m}$. (e) Chamber height profile of compressed circular flow-channel (side projection) and height contours corresponding to dark interferometry fringes (bottom projection). (f) Chamber height profile of compressed rectangular flow-channel (side projection) and height contours corresponding to dark interferometry fringes (bottom projection).

axis A ($1.41\ \mu\text{m}$ on minor axis B). This region can be extended to $1130\ \mu\text{m}$ on major axis and $1016\ \mu\text{m}$ on minor axis by using an auto-focus mechanism.

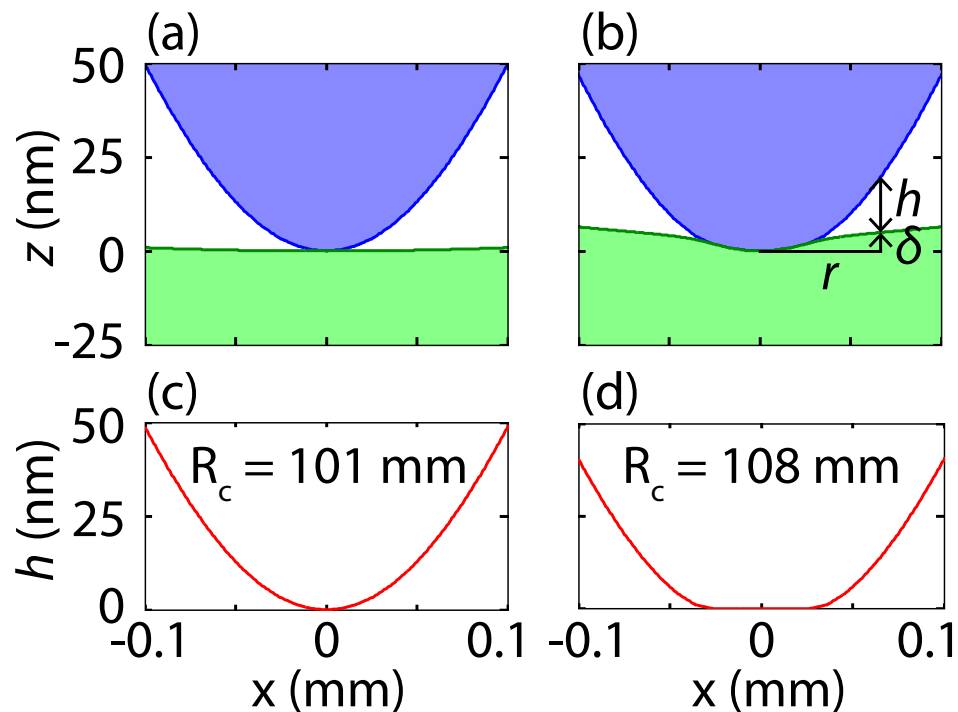


Figure 2-8: Schematic of the coverslip-coverslip contact point along the designated minor axis for the simulated circular chamber flow-cell. (a) Contact between the top (blue) and bottom (green) coverslips for over-push = $0 \mu\text{m}$. The bottom coverslip is slightly deformed. (b) Contact between the cover slips for over-push = $1 \mu\text{m}$. The quantities δ and h , as defined in the text, are shown as functions of the radius from the contact point r (c) Chamber height profile for over-push = $0 \mu\text{m}$ with radius of curvature computed from a quadratic fit performed inside the displayed region. (d) Chamber height profile for over-push = $1 \mu\text{m}$. The chamber is flat inside a region of contact with radius of curvature $r_b = 39 \mu\text{m}$ computed similarly.

$h_{\text{PDMS}}(\mu\text{m})$	push = 0 μm	1 μm	10 μm	push = 0 μm	1 μm		10 μm	
				R_c	R_c	r_b	R_c	r_b
10	1468 [1432]	1402 [1368]	1032 [1008]	424 [418]	440 [433]	62 [61]	454 [446]	106 [105]
30	753 [739]	743 [729]	660 [648]	149 [147]	153 [151]	39 [39]	157 [155]	70 [69]
50	560 [549]	555 [546]	516 [507]	92 [91]	94 [92]	29 [29]	96 [95]	62 [61]

Table 2–1: Circular flow-cell data for different film thicknesses h_{PDMS} . (Left) Radius of the region of focus (μm) along axis A [B]. (Right) Radius of curvature of the chamber R_c (mm) and region of contact r_b (μm) along axis A [B].

We define the imaging chamber radius of curvature, R_c , by fitting the chamber height profile to

$$h = r^2/(2R_c), \quad (2.1)$$

where h is the separation between the chamber walls and r is the radial distance from the contact point (Fig. 2–7 c). The circular chamber model is approximately radially symmetric, with percentage difference between its radii of curvature along axes A and B of 1% (Fig. 2–7 c, d). In contrast, the rectangular chamber is elliptical, with radius of curvature which is 14% larger along axis A than along axis B.

R_c decreases significantly as a function of increasing tape thickness and increases slightly as a function of over-pushing distance, as shown by Tables 2–1 (right section) and 2–2 (right section). The accessible range of radii of curvature (as large as 424 mm for a circular and 230 mm for a rectangular chamber) greatly exceed values accessible to lens-coverslip CLiC (a practical upper-limit for small-size commercial lenses is $R = 46$ mm for Thorlabs LA4600).

$h_{\text{PDMS}}(\mu\text{m})$	push = 0 μm	1 μm	10 μm	push = 0 μm	1 μm		10 μm	
				R_c	R_c	r_b	R_c	r_b
10	1026 [924]	1000 [903]	819 [754]	230 [201]	238 [207]	47 [45]	250 [214]	87 [83]
30	534 [494]	531 [492]	496 [462]	84 [74]	86 [75]	28 [26]	88 [77]	61 [59]
50	400 [374]	399 [372]	384 [360]	53 [46]	53 [47]	22 [22]	54 [48]	46 [44]

Table 2–2: Simulation data for rectangular flow-cells of different h_{PDMS} thicknesses. (Left) Radius of the region of focus (μm) along axis A [B]. (Right) Radius of curvature of the chamber R_c (mm) and region of contact r_b (μm) along axis A [B].

Model Geometry and Mesh

The simulation models were comprised of a spherical fused silica plano-convex push-lens (Thorlabs LA4966), two parallel glass coverslips coupled by a PDMS film (Young’s modulus of 1.96 MPa) and a rigid sample plate with a central hole (8.1-mm radius). For computational simplicity, the models did not include the sample fluid between the two coverslips that is free to exit the outlet during compression.

The model-meshes (Fig. 2–7 c,d) were fine-tuned to ensure convergence of results. The push-lens was modeled using a tetrahedral mesh, which became progressively more precise towards the center. The average element edge size was reduced from 216 μm to 4 μm near the contact point. The coverslips were modeled using a triangular surface mesh, which was swept through the bottom in equally spaced layers. The meshes included two layers on the top coverslip and three on the bottom coverslip. For the circular [rectangular] chamber model, the size of the average triangle-edge starts from 148 μm [138 μm] in the tape and chamber region, and decreases progressively from 103 μm to 23 μm [88 μm to 20 μm] within the three concentric circles shown, characterized by radii of 2 mm, 1 mm and 0.5 mm. The

mesh for the film was identical to the corresponding regions in the coverslips; the holder was also constructed using a tetrahedral mesh. The deformed chamber geometry, even close to the center, was shown to depend heavily on the resolution of the mesh outside the central precision circles. For each chamber geometry and film thickness, multiple simulations were performed with increasing mesh resolution until a convergent value for R_c was determined, presented in Tables 2-1 and 2-2.

2.4 Performance and Applications

2.4.1 CLiC Chamber Formation

In the following sections I present basic experiments which shows the basic capabilities of the CLiC devices. Figure 2–9 demonstrates the general CLiC experimental procedure used to apply a gradient of confinement to the imaging chamber. In this experiment the dual emission system is used to take both dye and fringe scans simultaneously. Once formed, the confinement gradient can be used to probe molecules in a number of ways [32, 37, 1, 36]. For example, in Section 2.4.2 we use this chamber characterization method to demonstrate molecular tracking at varying degrees of confinement.

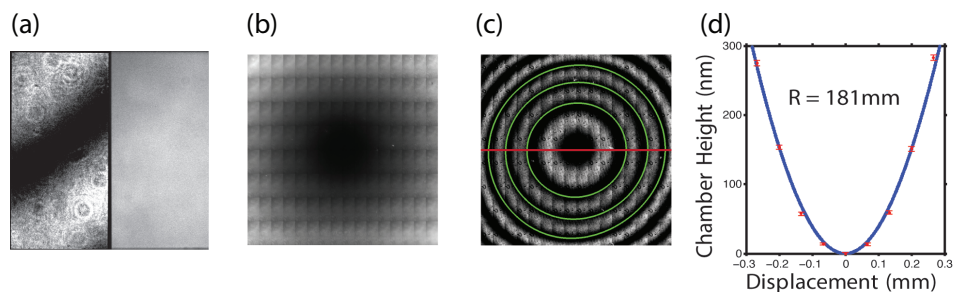


Figure 2–9: Method of chamber characterization utilizing the dual-channel imaging system. a) A single field of view when operating with the dual emission imaging system; left is an interferometry image using a 488 nm laser. The right side is an image of excited fluorescent dye (Alexa Fluor 647) using a 647 nm laser. b) and c) show the composed raster scans of the dye and interferometry respectively. Green contours were fit to the first three interference minima in c). From dye and interferometry data, a 2D cross section (along the red cut-line shown in c)) of the chamber geometry is made and shown in d). The red points represent the mean dye fluorescence intensity averaged over an 11x11 pixel region. The error bars represent the error of the mean of these points. From this cross section, the radius of curvature of the chamber, $R = 181\text{mm}$, can be determined from the quadratic fit (blue line).

Once contact has been made between the top and bottom coverslips, a typical field of view will appear as shown in Fig. 2–9 a). The 512×512 pixel image is divided in two by the dual-view system. The left half of the image is an interference pattern formed by a 488 nm laser reflecting from the top and bottom surfaces of the CLiC chamber. The optical path difference between the two coverslips creates an interference pattern known as Newton’s rings. The dark and light bands are regions of destructive and constructive interference. The right side of Fig. 2–9 a) is an image of excited fluorescent dye (Alexa Fluor 647).

To create a height profile map of the entire chamber geometry, a raster scan is taken over the desired region of the chamber. The two halves of the single field of view are composed into chamber maps of the interference pattern and dye intensity profile (shown in Fig. 2–9 b) and c) respectively). The dye intensity scales linearly with concentration. Due to the fact that all dye molecules within the chamber lie within the focal depth of the objective, we are able to infer that the dye intensity also scales linearly with height. This fluorescent dye intensity is fit with a polynomial in order to obtain a function proportional to the local chamber height. This height function is then scaled to represent an absolute chamber height using the information obtained through interferometry; specifically, by using the interference minima which appear at heights given by $h = \frac{m\lambda}{2n\cos(\theta)}$, where m is a positive integer, λ is the wavelength of the laser, n is the index of refraction of the sample and θ is the angle of the incoming beam from the vertical axis – typically this is 45 degrees.

Figure 2–9 d) shows a 2D cross section of the chamber geometry which is taken along the red cut-line shown in c). The chamber height function along this line is fit

with a quadratic function from which the radius of curvature of the chamber, R , is then extracted. In the particular case shown in Figure 2–9 d), $R = 181\text{mm}$.

2.4.2 Particle Tracking

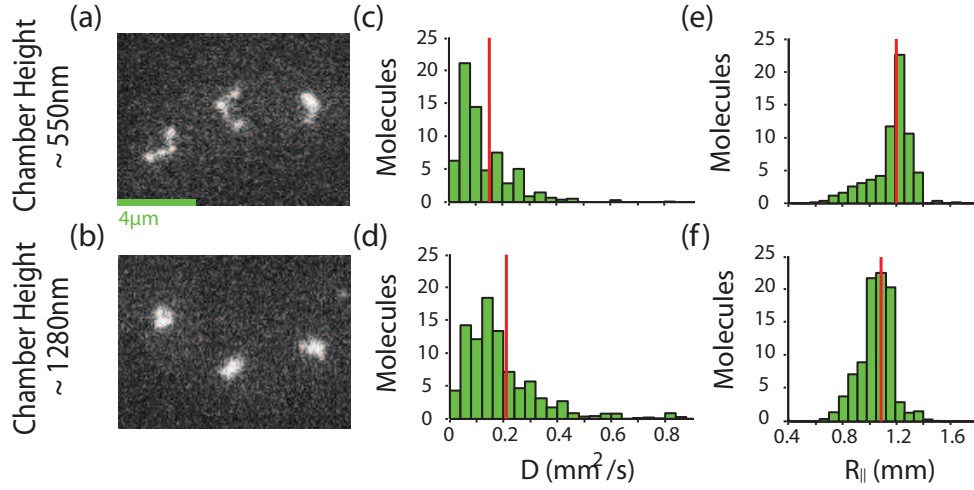


Figure 2–10: Diffusion coefficients and in-plane radius of gyration of λ -phage DNA molecules. a) & b) Images of fluorescently labeled DNA molecules at heights of $H \approx 550\text{ nm}$ and $H \approx 1280\text{ nm}$ respectively. c) & d) Histograms of diffusion coefficients, D , for freely-diffusing molecules. The mean values (designated by red lines) are $0.18 \pm 0.02\ \mu\text{m}^2/\text{s}$ (550 nm) and $0.23 \pm 0.02\ \mu\text{m}^2/\text{s}$ (1280 nm). e) & f) Histograms of in-plane radius of gyration, $R_{||}$. Mean values are $1.20 \pm 0.22\ \mu\text{m}$ (550 nm) and $1.1 \pm 0.14\ \mu\text{m}$ (1280 nm).

In order to demonstrate CLiC as a platform for nanoscale confinement spectroscopy we tracked single freely diffusing λ -phage DNA molecules. We then compared the diffusion coefficients of these molecules at two different regions of confinement within the sample chamber,

Figure 2–10 a) and b) present fluorescent images of freely diffusing λ -phage DNA molecules stained with YOYO-1 fluorescent dye. The flow-cell chamber heights for the molecules shown and analyzed lie between 460–640 nm and 1100–1470 nm. The larger height is approximately equal to the bulk radius of gyration, R_g , of the molecules. Polymer chains generally [38], and DNA in particular [39], have been shown to experience the effects of confinement at heights $\lesssim 2R_g$. Therefore, the molecules are confined for both ranges of chamber heights with stronger confinement effects at the smaller chamber height. The corresponding trajectory analysis and the distribution of diffusion coefficients, D , shown in Fig. 2–10 c), d), demonstrate the effect of the imposed confinement in slowing DNA diffusion. Similarly, at these heights we measured the in-plane radius of gyration:

$$R_{\parallel} = \sqrt{\frac{\sum_i (\mathbf{r}_i - \bar{\mathbf{r}})^2 I_i}{\sum_i I_i}}, \quad (2.2)$$

which measures the square root of the mean squared distance from the centroid of the particle, $\bar{\mathbf{r}}$, weighted by the pixels' intensities, I . Figure 2–10 e), f) demonstrate an increase in the in-plane radius of gyration with greater confinement. All molecules were tracked for a total of 55 seconds (1000 frames). Figure 2–10 c), d) are based on 66 and 92 lifetime-weighted particles respectively.

For the preparation of the sample shown in Fig. 2–10, the following experimental methods were followed. The final concentrations of reagents were 1.445 mM Tris base, 0.445 mM boric acid, 0.1 mM EDTA, 0.32 mM HCl, 577 nM Alexa Fluor 647, 285 mM 2-mercaptoethanol, and 13 pM of YOYO-1 fluorescently stained λ -DNA at a labeling ratio of one fluorophore per 10 base pairs. This solution had a final pH of 7.1 and an ionic concentration of 1.35 mM. Coverslips for all experiments were cleaned using 2:1 sulfuric acid to 30% hydrogen peroxide solution (piranha) for 45 minutes. The coverslips were then treated with 1M KOH for 15 minutes, rinsed thoroughly with deionized water, and dried before being assembled into a flow-cell.

Molecule Tracking and Analysis Methods

Molecules were identified by a 4-step process. First, pixels were converted to binary values about a threshold that was chosen to eliminate anything but lambda DNA. Then a series of image-processing operations (using the Matlab command “bwmorph”) were used to clean up the image and identify molecules (1 quorum fill, 3 dilations, and 2 erosions). Analysis parameters were chosen so as to minimize the loss or double-identification of dim sections of elongated molecules.

Once the molecules were located in each frame, the intensity-weighted centroid for each molecule was computed using the Matlab command “regionprops”. Movies were manually examined for misattributed centroids owing to two particles in proximity being identified as one, or a single particle being assigned two centroids. The centroids were then linked between frames to form particle trajectories. Only trajectories longer than 2.7 s (50 frames) were included in the results presented in Fig.

2–10. Particle trajectories were plotted on top of their respective movies and erroneous parts of trajectories were eliminated manually.

The mean diffusion coefficient and mean in-plane radius of gyration for a given set of particles was weighted by the particles' lifetimes. Uncertainty in D , R_{\parallel} , and in their respective ratios for different heights, $D(550\text{nm})/D(1280\text{nm})$ and $R_{\parallel}(550\text{nm})/R_{\parallel}(1280\text{nm})$, span a 95% confidence interval using 10,000 bootstrap re-samples.

CHAPTER 3

Home-Built Fluorescence Microscope (HBM)

The next major instrumentation design involved the creation of an open-frame home-built inverted fluorescence microscope.

3.1 Introduction and Motivation for the Home-Built Microscope

The creation of the home-built Fluorescence Microscope (HBM) arose from a real need within our laboratory to create a cost effective and versatile microscopy station which was easily customizable. While there is no shortage of commercially available microscopes, there are significant limitations to using most “off-the-shelf” microscope and imaging systems. Many have a closed-box design that limits the ways in which they can be used. This often makes it difficult to develop custom experimental devices that integrate with the system. To overcome these challenges, I have created a versatile, open-frame, inverted fluorescence microscope system, which includes a laser excitation and a dual-emission imaging system. The open frame allows for the introduction of new devices, facilitates diagnostics and allows further modular additions to be made independently.

Matthew Tarling, an undergraduate student who did his bachelor thesis with the Leslie Lab, originally began this project in collaboration with Richard Talbot. After Matthew’s departure I adopted the project and redesigned, tested and calibrated the microscope to account for a number of design flaws that had limited the contrast and resolution. Upon the successful implementation of the microscope, the work

was published in the Review of Scientific Instruments in a paper titled “Open-Frame System for Single-Molecule Microscopy” [2].

In addition to the material contained in this section, this paper includes the manual CLiC device (shown in Section 2.1) as a modular add-on for our microscope. It was our interest to publish the HBM along with a CLiC device that suited the microscope in character and design - in other words, affordable and simple, yet powerful. Coupling the open-framed microscope with a manual version of a CLiC allowed us to present a versatile and powerful single-molecule microscopy station to interested researches through our publication. The remaining sections demonstrate the design, construction and capabilities of the HBM itself.

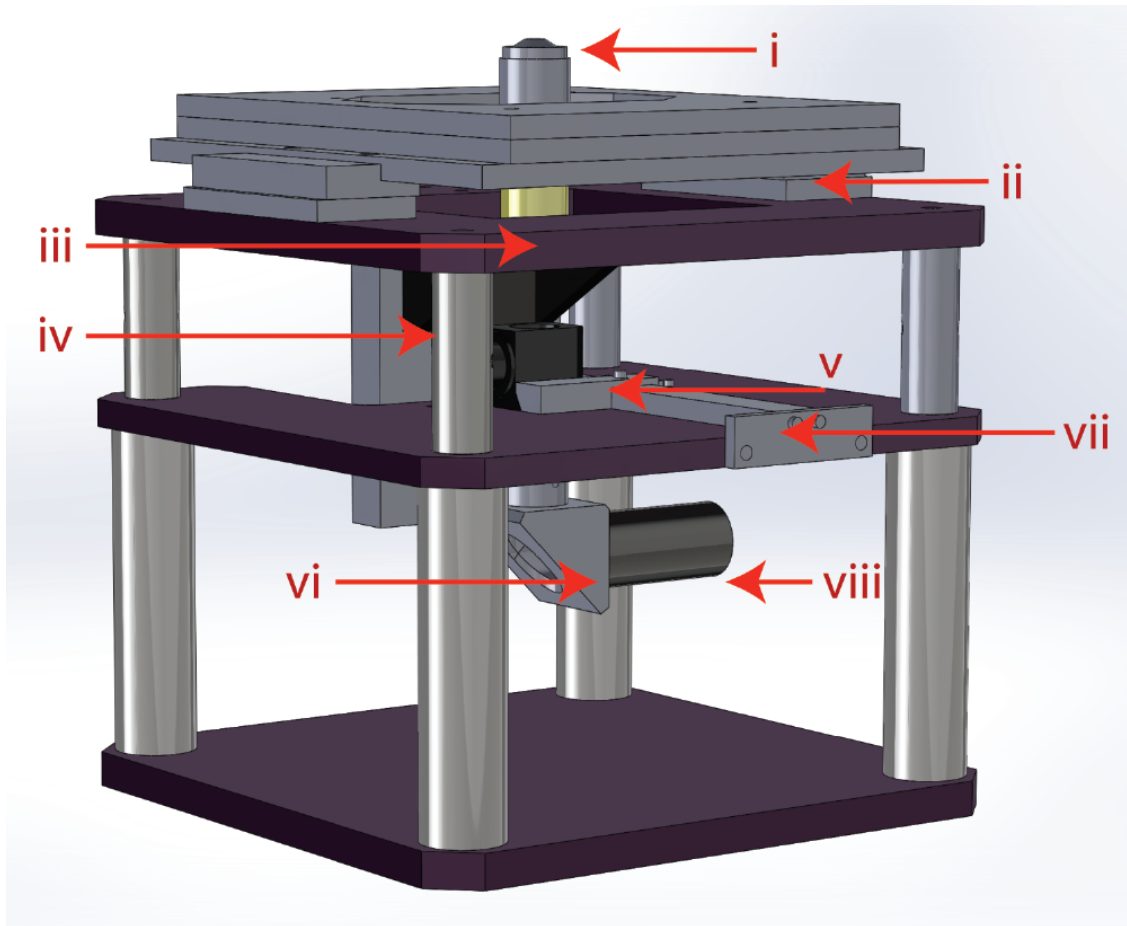


Figure 3–1: Schematic of the microscope chassis. The labeled parts are as follows: i) objective; ii) X-Y stage; iii) objective collar; iv) motorized lens positioner; v) dichroic; vi) rotating mirror; vii) tube (with tube lens); viii) dichroic slider mount. For a full list of custom parts see Table 3–1.

3.2 Custom Microscope

The current version of the inverted microscope chassis is shown in Fig. 3–1. Its open-frame concept allows for integration with experimental devices and customization of optical components. The microscope is the base unit for the microscopy system which was designed to integrate with the manual CLiC device (see Section

2.1) and two-colour imaging system presented in the following sections. It also functions independently as an inverted fluorescence microscope for widefield or TIRF imaging.

The microscope chassis physically consists of three plates constructed from aluminum tooling plate for precisely parallel faces. These bottom and middle plates are separated by four 1.5"-diameter stainless steel pillars and the middle and top are separated by four 1"-diameter stainless steel pillars. The bottom plate serves as a base for the structure. The top of the center plate supports the dichroic cube holder assembly. The dichroic holder functions by allowing an adjustable slider to lock in place, which is compatible with most commercially available mounted dichroics. A mirror and tube-lens assembly attaches to a 90-degree adjustable turret that is mounted on the bottom of the center plate. The rotating turret allows the user to direct the fluorescence to one of two imaging systems: either directly to an EM-CCD camera or to a two-color imaging system (outlined in Section 3.4). The top plate supports the objective focusing assembly as well as an X-Y translation stage. The objective is mounted on a motorized lens positioner, which allows for precise focusing. For a list of all custom machined parts see Table 3-1.

The modular design of this microscope allows for variability in features and cost. For example, if the option to switch emission pathways quickly is not required, the rotating turret can be removed. Additionally, an optical encoder used for precise measurements of the objective's position is recommended for many applications but not required for basic microscopy.

Table 3–1: Custom Components of Chassis

Description	Quantity	Materials
Aluminum Base Plate	3	Aluminum Tooling Plate
Rotation Turret	1	Brass, 6061 Aluminum
Dichroic Holder Assembly	1	6061 Aluminum
Tube Lens Support	1	6061 Aluminum

3.3 Excitation Optics

A simplified schematic of the excitation pathway is shown in Fig. 3–2. The beams exit the three lasers (488 nm, 561 nm, and 647 nm) before two long-pass dichroics combine them into a single beam. Once combined, the beam passes through two sets of telescopes that each consists of two lenses separated by their back focal lengths. Together, the two telescopes expand the beam by a factor of ~ 45 . The first telescope is made from lenses with focal lengths of 50mm and 150mm and the second from lenses with focal lengths of 50 mm and 750 mm. This magnification allows the lasers to uniformly illuminate the full field of view.

Finally, the combined beams pass through the wide-field lens, which focuses the light on the back focal plane of the objective. The wide-field lens is mounted on a micrometer-driven stage that serves as the base for the final mirror and lens assembly. This assembly controls the position at which the beam hits the dichroic and, ultimately, the angle at which it falls incident on the sample, allowing total internal reflection fluorescence microscopy to be performed.

This excitation setup allows the use of high-powered lasers (~ 120 mW) to excite single molecules allowing for short exposure times. The beam pathway was simulated and optimized for chromatic shift using OSLO optical design software. Optics were chosen to minimize the chromatic focal shift between the three lasers. The final setup has a maximum focal shift of 0.01 mm between the blue and green lasers and 0.56 mm between the blue and red lasers. This allows the beam to be sufficiently expanded for all three wavelengths at a single focal height.

The open-frame concept of the excitation system allows for significant customization. For example, the lasers can be blocked independently using shutters placed in front of the combining dichroics or shared between two separate microscopes through the use of a beam splitter. More components, such as an acousto-optic tunable filter (AOTF), can be added into the excitation pathway to allow for techniques such as Fluorescence Resonance Energy Transfer with Alternating Laser Excitation (FRET-ALEX) [40] or super resolution techniques such as Stochastic Optical Reconstruction Microscopy (STORM) [11]. The customizability of the microscope also makes it suitable for use with multiple imaging techniques at once (e.g. combining fluorescence with polarization optics to incorporate measurements of molecular orientations and rotational dynamics [41]).

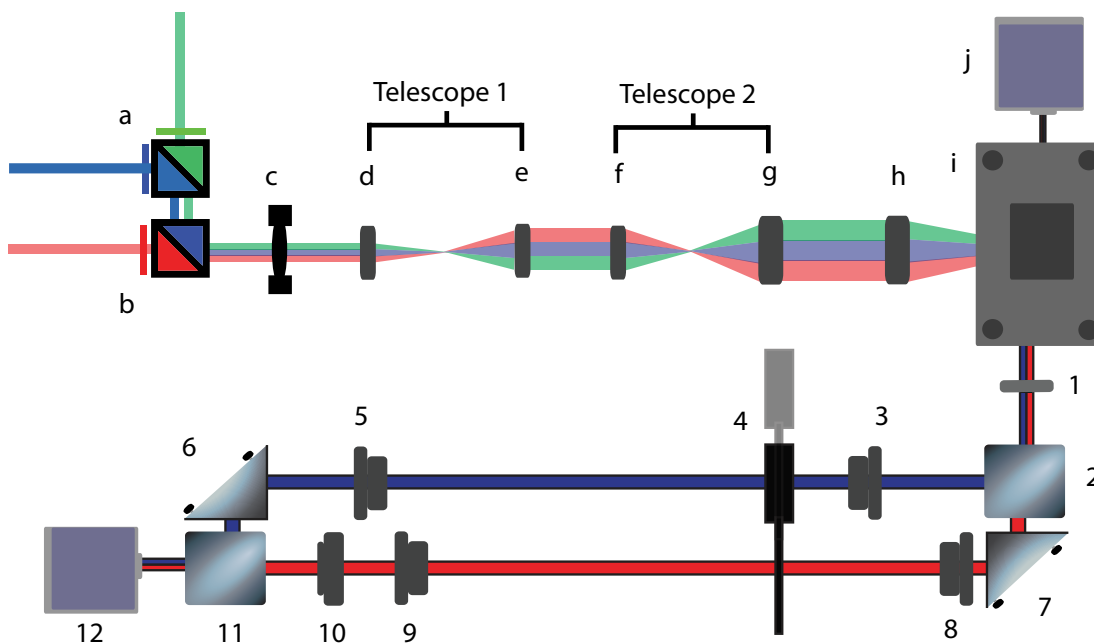


Figure 3–2: Excitation and dual-emission optical pathways: The top pathway is a simplified schematic of the excitation optics. a-j represents the emission pathway where the laser beams are combined and expanded before entering the microscope. 1-12 represents the dual-emission imaging pathways where the image is split according to wavelength and recombined side-by-side on the camera. For a complete parts list of both pathways see Table 3–2. Note: the two systems are not shown to scale with respect to each other.

3.4 Dual-Channel Imaging System

For many experiments, it is crucial to be able to simultaneously label and image more than one molecular species using spectrally distinct probes. As is the case with most commercially available microscope chassis, two-color imaging systems often have a closed-box design which typically restricts the choice of spectra and may not allow for the spectra of each channel to be controlled independently during an experiment. The custom dual-emission imaging system that I have created as

part of our microscopy system overcomes these limitations through its open and customizable design.

Light collected from the objective can be sent to the dual-emission imaging system by rotating the lens tube using its rotation turret. This setup allows for quick and easy switching between single-view and dual-view experiments. Our dual-emission imaging station (Fig. 3-2, 1-12) is made from simple, off-the-shelf components. The system uses optical elements with a 2"-diameter in order to reduce aberrations and custom emission filters to control the spectra viewed in each channel.

The dual emission system functions by creating two spectrally distinct images of the same field of view and allows them to be viewed simultaneously on the same CCD chip. The dual imaging system achieves this by placing a physical slit at the first imaging plane. This slit cuts the image to half the size of the camera's CCD chip (8.12 mm by 4.06 mm for an Andor iXon camera). Wavelengths above and below the dichroic's characteristic wavelength are directed to separate optical paths, forming two spectrally distinct images. The choice of the dichroic's transmission spectrum depends on the fluorophores being imaged. The transmitted and reflected paths each contain two identical lenses that are separated by their focal lengths. The system is designed to use two lenses to focus the image rather than one, as our simulations showed that this setup reduces chromatic and spherical aberrations. Each path has a single mirror that allows the two images to be positioned side-by-side before they are recombined into a single beam by a second dichroic. For a list of all components used in the excitation and emission pathways, see Table 3-2.

Table 3–2: List of Optical Components Shown in Figure 3–2

Excitation Pathway		Emission Pathways	
Position	Description	Position	Description
a	561 nm Dichroic	1	Adjustable Mechanical Slit
b	488 nm Dichroic	2	640 nm Dichroic
c	Filter Wheel	3	Lens
d	1 st Lens of 1 st Telescope	4	Emission Filter (on Slider)
e	2 nd Lens of 1 st Telescope	5	Lens
f	1 st Lens of 2 nd Telescope	6	2" Mirror
g	2 nd Lens of 2 nd Telescope	7	2" Mirror
h	Widefield Lens	8	Lens
i	Custom Microscope	9	Lens
j	EMCCD Camera	10	Emission Filter
		11	640 nm Dichroic
		12	EMCCD Camera

The dual emission imaging system can be easily modified to allow the use of a wide range of fluorophores by placing the dichroics on magnetic mounts, allowing them to be easily exchanged between experiments. The open design of the dual imaging system also allows for emission filters to be placed in specific imaging pathways rather than having many two-band pass emission filters in a conventional dichroic

turret. The emission filters can also be mounted on sliders, allowing for quick insertion or removal of the filters (Fig. 3-2). This is particularly useful for experiments performed using CLiC microscopy where interferometry (direct imaging of the exciting laser) is used to measure the chamber's height profile [32, 1, 37, 36].

3.5 Performance and Applications

3.5.1 Single-Molecule Photo Bleaching

In order to demonstrate a number of the versatile capabilities of our microscopy system, we have taken a series of demonstration data. To demonstrate the single-molecule imaging capabilities of the microscope, we observed streptavidin singly labeled with Alexa Fluor 488 fluorescent dye (Life Technologies). The molecules were diluted to 180pM in phosphate buffered saline solution (PBS), with a pH of 7.74. The streptavidin molecules were bound to the bottom coverslip of the flow-cell using a polyethylene glycol (PEG) coating comprising 1% biotinylated PEG [42].

A flow-cell was formed with 30 μ m-thick double-sided tape with the PEG-coated coverslip on the bottom, and a coverslip cleaned with piranha solution (3:1 H₂SO₄: 30% H₂O₂) on the top. While being observed on the microscope, labeled streptavidin was flowed into the sample chamber and allowed to bind with the biotin. After 10-15 minutes excess streptavidin was washed out. While the bottom coverslip was in focus, the laser beam angle was altered until total internal reflection occurred and single molecules could be seen clearly. Video was taken at 200 ms exposure and 7.5 mW of 488 nm laser power. All images were taken with an Andor iXon3 897 EMCCD with 16 bit Precision. A cropped image (115 \times 115 pixels) of streptavidin molecules taken through the short path of the dual-emission imaging system can be seen in Fig. 3-3 a).

Observing intensity traces of individual particles showed clear photo bleaching steps. Figure 3-3 b) shows the intensity of the single molecule within the red circle shown in a) vs. time, normalized by the background intensity. The molecule was

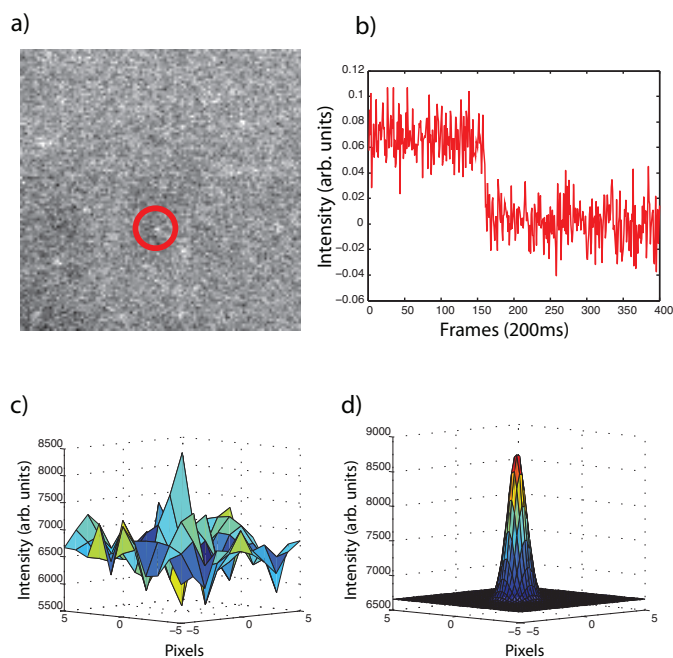


Figure 3-3: Single molecules blinking to background taken with the home-built microscope using TIRF. (a) Image of a 115x115 pixel field of view of streptavidin molecules fluorescently labeled with Alexa Fluor 488 bound to a biotinylated-PEG coating of a coverslip. (b) A background normalized intensity vs. time plot of a singly-labeled molecule (circled in red in a)) which undergoes a single photo bleaching step. (c) Raw intensity data of the molecule highlighted in a). (d) Raw data shown in c) fit to a Gaussian function with standard deviation of 0.6 and 0.5 pixels in x and y respectively.

observed for 400 frames at 200 ms/frame. The molecule bleaches at frame ~ 160 after which the intensity drops to the levels found at background, which verifies that the molecule is singly labeled. The point-spread function (PSF) of this molecule was analyzed in c) and d): the former is the raw intensity data of the individual molecule and the latter is this data fit to a Gaussian function. The Gaussian fit has a standard deviation of 0.62 ± 0.8 pixels in X and 0.58 ± 0.8 pixels in Y. For

particles emitting at 525 nm, and a 60X objective with a numerical aperture (NA) of 1.49 (Nikon Apochromat TIRF) the Abbe diffraction-limited radius is ~ 0.66 pixels.

3.5.2 FRET With Dual-Channel Imaging

To demonstrate the capabilities of the dual-channel imaging system we present a basic Förster Resonance Energy Transfer (FRET) experiment. FRET is a technique which uses a pair of complementary fluorophores to detect when two molecules have reached close physical proximity (~ 10 nm or less) [43]. This technique works for fluorophore pairs in which the “donor” fluorophore’s emission spectrum overlaps with the absorption spectrum of the “acceptor” fluorophore. For suitable fluorophores, energy from the donor fluorophore is transferred to the acceptor fluorophore through dipole-dipole interactions. This allows the acceptor to fluoresce even though it does not receive energy directly from the excitation laser.

In our demonstration experiment, small oligonucleotides are bound to a chamber that is passivated with PEG, as in Section 3.5.1. Short oligonucleotides were bound to this surface through a biotin-streptavidin bond. These DNA segments were labeled with Cy5 (depicted in Fig 3-4 a)). Once bound, complementary oligonucleotides, which were labeled with Cy3, were flowed into the flow-cell. These complementary oligos selectively bound to the immobilized oligos in such a way as to bring the Cy3-Cy5 FRET pair into close proximity. The sample was excited with green laser light (561 nm) and a FRET signal was observed in a fraction of the molecules. A schematic of this FRET interaction between bound oligos is shown in Fig 3-4 b)).

The dual-channel imaging system allows for viewing both the donor and acceptor fluorophores simultaneously in separate channels. Figure 3-4 c) shows a small region

(140 by 100 pixels) of both channels. Within this region immobile oligos that do not have a complementary oligo bound to them fluoresce only in the “green” channel (the molecules circled in yellow in Fig 3–4 c)) and schematically depicted in 3–4 b-ii), while those that do have a bound oligo fluoresce in both channels (circled in blue and depicted in 3–4 b-i)).

Molecules which showed a FRET signal had their intensities tracked over time and were found to photo bleach in both channels at the same frame. These instances were taken to represent single donor fluorophore photo bleaching, which simultaneously extinguishes the acceptor. The lifetime intensities of the two fluorophores in Fig 3–4 c) showing this phenomenon (circled in blue) are shown in Fig 3–4 d). Signal cross-talk between channels was shown to be insignificant as the oligos without FRET pairs (yellow circles) did not appear in the red channel.

The exact procedure for the experiment was as follows: Streptavidin in a buffer of 10 mM Tris-HCl, 100 mM NaCl, and 0.05% Tween-20 was flowed into the chamber, allowed to sit for 5 minutes, and then washed out with 200 μ L of the buffer. The Cy5 labeled oligo (5-/5Cy5/ACCTCGCGACCGTCGCCA/3BiodT/-3, purchased from IDT), at a concentration of 10 pM in a conjugation buffer of 10 mM Tris-HCl, 1.0 nM EDTA, and 2.0 M NaCl was flowed in, allowed to incubate, and then washed out with 200 μ L of 10 mM Tris-HCl. Lastly, the complementary oligo with a Cy3 label, (5-TGGCGACGGTCGCGAGGT/3Cy3Sp/-3, also purchased from IDT) was flowed in at a concentration of 1 nM in 10 mM Tris-HCl. The reagents were allowed to incubate for 15 minutes, and then washed out with 400 μ L of buffer. 10 mM TrisHCl including protocatechuic acid and protocatechuate-3,4-dioxygenase, a deoxygenation

system, was flowed in and allowed to act on the buffer in darkness for 30 minutes. Images were acquired using total internal reflection illumination with 300 EM gain and a 100 ms exposure time.

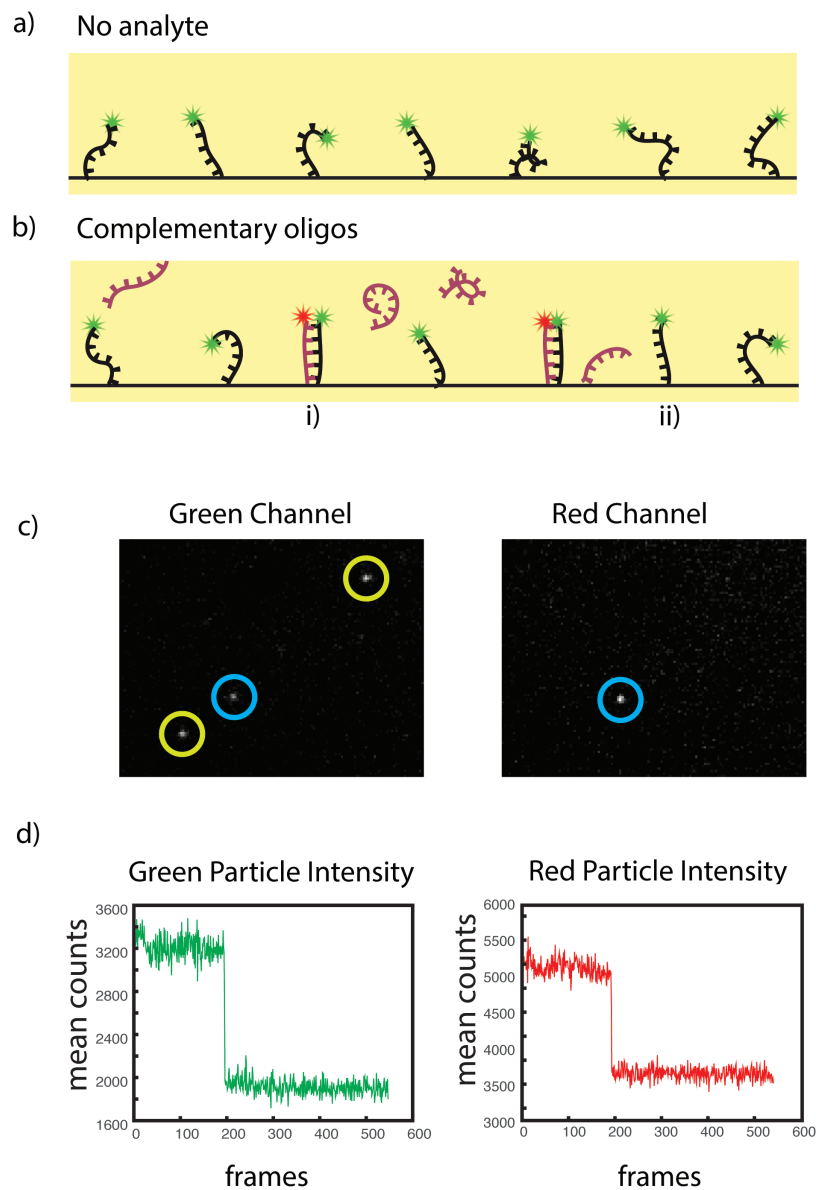


Figure 3–4: FRET assay using bound oligonucleotides labeled with Cy5 and complementary oligo labeled with Cy3. a) represents oligos bound to the PEGylated surface with a streptavidin-biotin bond and excited with a 561 nm laser. b) represents the above after the complementary oligos have been introduced. b-i represents two oligos which bind and produce a FRET signal, while b-ii represents an oligo with no complement and only fluoresces as in a). In c) a 140 by 100 region is shown where three bound molecules are fluorescing in the green channel, and one in the red channel. The yellow circles correspond to single oligos shown in b-ii, while the green circle corresponds to a FRET pair as in b-i. d) shows the mean counts of the particle circled in green over 550 frames in both the green and red channels. In both channels the intensity drops to background in a single frame demonstrating that the FRET donor fluorophore has bleached.

CHAPTER 4

Conclusions and Future Directions

4.0.3 Conclusions

In this thesis I have demonstrated a number of the projects in which I have been involved with throughout my masters research. As the first graduate student in an experimental laboratory, my work has focused on instrumentation design and development. In the First section, I have demonstrated the construction and operation of a powerful and accessible single-molecule microscopy CLiC devices. These devices extend single-molecule microscopy to a much wider range of reagent concentrations and observation timescales than standard techniques can access, and serves as a novel platform for nanoscale confinement experiments. To understand and optimize the operation and geometry of this nanoscale device, we have created and tested a predictive model of the flow-cell CLiC imaging chamber geometry.

The use of the CLiC device's ability to tune interactions between molecules through varying levels of confinement is transferable to the fields of nanotechnology, materials science, and chemistry [44]. The imaging benefits delivered by flow-cell CLiC microscopy are transferable to many fields of research. For example, CLiC imaging can be used to shed new light into the molecular underpinnings of the emergent phenomenon of active matter, a new area of soft-materials research [35].

Single-molecule measurements of the protein-polymer and polymer-polymer interactions driving these macroscopic dynamic systems are lacking, which must be examined away from surfaces due to depletion effects, for which CLiC imaging is ideally suited.

In the second main section of this thesis, I have presented the design and construction of a versatile open-frame fluorescence microscopy system and have demonstrated a number of applications for wide-field and single-molecule fluorescence experiments. We have shown our system's dual-channel imaging system allows for imaging between spectrally distinct channels. The microscopy system's open frame offers many advantages to systems which are sold as sealed "black boxes." The design of the microscope and optical pathways allows access to the beam at all points, easing troubleshooting and setup, and allows for the customization and easy expansion of the system.

4.0.4 Future Directions

The MadCity CLiC instrumentation device has already been further modified, and a new version, CLiC 3.0, has been created. This model, developed by Dan Berard, maintains the open concept but miniaturizes the device. CLiC 3.0 is the current CLiC device operating on one of the microscope stations and is set to replace the CLiC device on another. The MadCity device will remain functional and operate as the CLiC device for the third microscopy station within the Leslie lab. We have also recently created a temperature control system to incorporate with these CLiC devices. Originally we had tested a fluid based temperature control system that pumped water through copper tubes embedded within an objective collar and

sample plate. We found that unfortunately, this device lacked the precision and stability required for our measurements. The two pieces, though heated and cooled by the same fluid source, could not maintain the same temperature, which caused temperature gradients within the sample. An updated electronic cartridge heater system with PID feedback control has been designed by Dan Berard to replace the fluid based system. This heating device will integrate with the MadCity device and is currently being tested and calibrated. We plan to publish this integrated system in a manuscript currently under production in the Review of Scientific Instruments.

The HBM microscope has undergone a series of modifications. A summary can be seen in Fig. 4-1. The original device (Fig. 4-1, a)) was created with equal separation between microscope plates which offered ease of access to the dichroic and objective – however, we found in this configuration the distance created caused the tube lens to be overfilled with light resulting in a loss of image quality. These issues were corrected and this configuration of the microscope was then published (Fig. 4-1, b)). We have since found a few areas in which further improvements were possible. Namely, we identified that diffuse light may be reflecting to the camera. For this reason all parts will be sandblasted to produce a matt finish and then anodized black in order to stop reflections of stray-light. Also, modifications to allow greater ease of use have been redesigned. These include a new dichroic holder with a spring loaded ball bearing positioner for greater stability and precision when changing dichroics, and a new rotation device with magnetic locks.

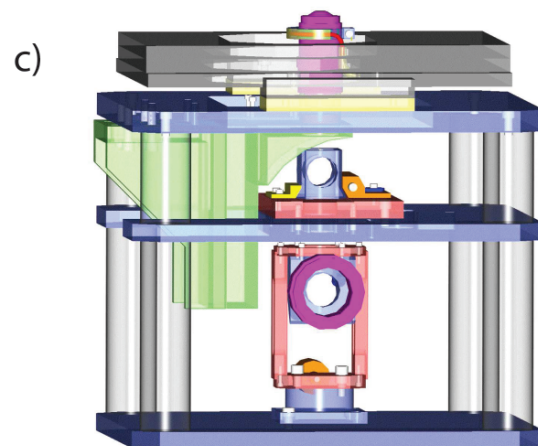
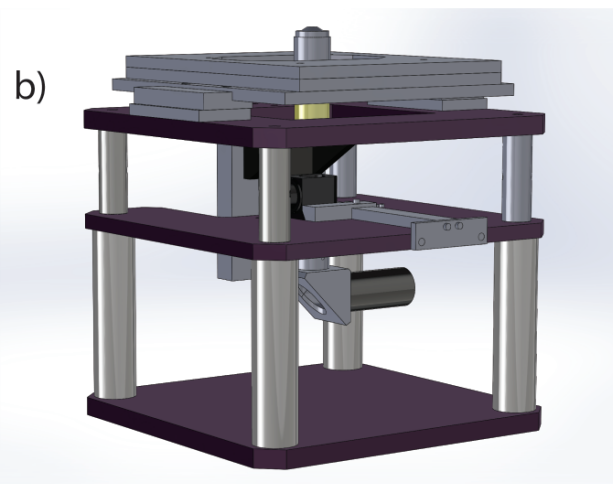
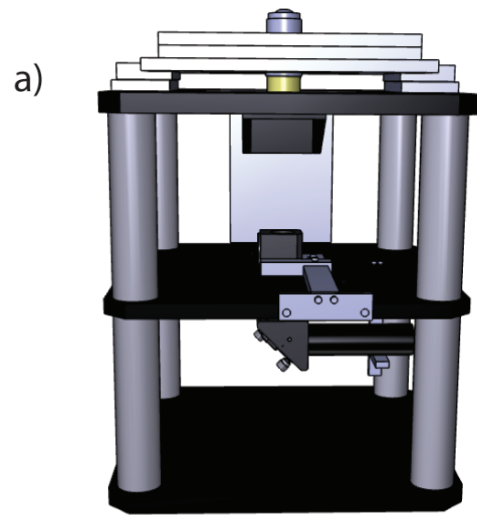


Figure 4–1: Evolution of the HBM. a) The original implementation of the microscope. b) the modified microscope which was published in Rev. Sci. [2]. c) Further proposed modifications

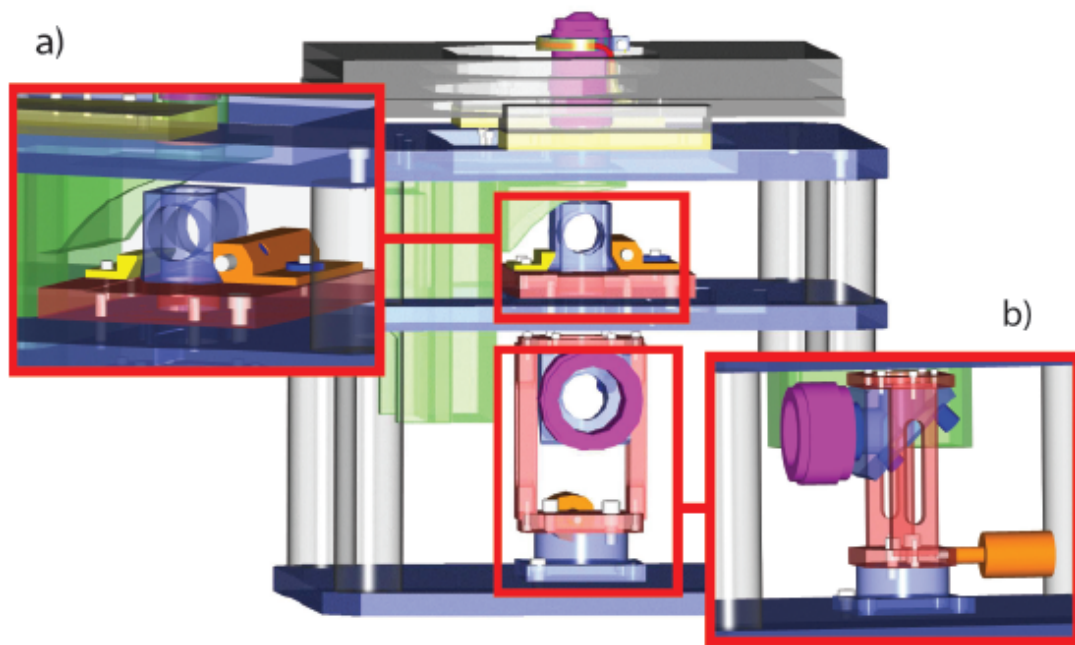


Figure 4-2: Further planned modifications to the home-built microscope. a) demonstrates a modified dichroic holder for enhanced stability, repeatability in placement and ease of use. b) Represents a modified mechanism for the rotation device featuring a magnetic locking mechanism.

REFERENCES

- [1] D. Berard, C. M. J. McFaul, J. S. Leith, A. Arsenault, F. Michaud, and S. R. Leslie. Convex lens-induced nanoscale templating. *Rev. Sci. Instrum.*, 84:103704, 2013.
- [2] A. Arsenault, J. S. Leith, G. Henkin, C. M. J. McFaul, M. Tarling, R. Talbot, D. Berard, F. Michaud, S. Scott, and S. R. Leslie. Open-frame system for single-molecule microscopy. *Review of Scientific Instruments*, 86:033701, 2015.
- [3] B. Jia F. Michaud A. Arsenault A. Martin D. Berard S. R. Leslie C. M. J. McFaul, J. S. Leith. Single-molecule microscopy using tunable nanoscale confinement. *SPIE Conference Proceeding*, 8811, 2013.
- [4] A. V. Helden, S. Dupre, and R. V. Gent. *The Origins of the Telescope*. KNAW Press, Cambridge MA, 2010.
- [5] M. Wainwright. An alternative view of the early history of microbiology. *Advances in Applied Microbiology.*, 53:333–355, 2003.
- [6] K. Chang. 2 americans and a german are awarded nobel prize in chemistry. New York Times. Retrieved October 8, 2014. Available at <http://www.nytimes.com/2014/10/09/science/nobel-prize-chemistry.html>.
- [7] E. Hecht. *Optics*. Addison Wesley, San Francisco, 4ed edition. pg. 617.
- [8] M. Abramowitz and M. W. Davidson. Olympus microscopy resource center: Mechanical tube length. Available at <http://www.olympusmicro.com/primer/anatomy/tubelength.html> (2015/02/12).
- [9] Rayleigh L. Investigations in optics, with special reference to the spectroscope. *Philosophical magazine*, 5 8 (49):261274, 1879.
- [10] M. Abramowitz and M. W. Davidson. Olympus microscopy resource center: Numerical aperture and resolution. Available at <http://www.olympusmicro.com/primer/anatomy/numaperture.html> (2015/02/12).

- [11] B. Huang, M. Bates, and X. Zhuang. Super resolution fluorescence microscopy. *Annu Rev Biochem*, 78:993–1016, 2009.
- [12] S. W. Hell and J. Wichmann. Breaking the diffraction resolution limit by stimulated emission: stimulated-emission-depletion fluorescence microscopy. *Optics Letters*, 519:780–782, 1994.
- [13] U. Drig, D. W. Pohl, and F. Rohner. Nearfield optical scanning microscopy. *J. Appl. Phys.*, 59:3318, 1986.
- [14] S. W. Hell and J. Wichmann. Multicolor super-resolution imaging with photo-switchable fluorescent probes. *Optics Letters*, 519:780–782, 1994.
- [15] E. Betzig, G. H. Patterson, R. Sougrat, O. W. Lindwasser, S. Olenych, M. W. Davidson, J. S. Bonifacino, J. Lippincott-Schwartz, and H. F. Hess. Imaging intracellular fluorescent proteins at nanometer resolution. *Science*, 313:5793, 2006.
- [16] C. J. Cogswell and C. J. R. Sheppard. Confocal differential interference contrast (dic) microscopy: including a theoretical analysis of conventional and confocal dic imaging. *Journal of Microscopy*, 165:81–101, 2011.
- [17] C. R. Burch and J P P Stock. Phase-contrast microscopy. *Journal of Scientific Instruments*, 19:71, 1942.
- [18] J. G. White, W. B. Amos, and M. Fordham. An evaluation of confocal versus conventional imaging of biological structures by fluorescence light microscopy. *J Cell Biol.*, 105(1):41–48, 1987.
- [19] D. M. Shotton. Confocal scanning optical microscopy and its applications for biological specimens. *J. Cell. Sci.*, 94:175–206, 1989.
- [20] D. Axelrod, T. P. Burghardt, and N. L. Thompson. Total internal reflection fluorescence. *Annual Review of Biophysics and Bioengineering*, 13:247–268, 1984.
- [21] W. E. Moerner. A dozen years of single-molecule spectroscopy in physics, chemistry, and biophysics. *J. Phys. Chem. B*, 106:910–927, 2002.
- [22] K. Kneipp, Y. Wang, H. Kneipp, L. T. Perelman, I. Itzkan, R. R. Dasari, and M. S. Feld. Single molecule detection using surface-enhanced raman scattering (sers). *Phys. Rev. Lett.*, 78:1667, 1997.

- [23] F. Kulzer and M. Orrit. Single-molecule optics. *Ann. Rev. Phys. Chem.*, 55:585–611, 2004.
- [24] T. H. Lee, J. I. Gonzalez, J. Zheng, and R. M. Dickson. Single-stranded dna curtains for real-time single-molecule visualization of protein-nucleic acid interactions. *Anal Chem.*, 38:534, 2005.
- [25] W. E. Moerner. New directions in single-molecule imaging and analysis. *Proceedings of the National Academy of Sciences*, 104(31):12596–12602, 2007.
- [26] C. Joo, H. Balci, Y. Ishitsuka, C. Buranachai, and T. Ha. Advances in single-molecule fluorescence methods for molecular biology. *Annual Review of Biochemistry*, 77(1):51–76, 2008.
- [27] A. Jain, R. Liu, B. Ramani, E. Arauz, Y. Ishitsuka, K. Ragnathan, J. Park, J. Chen, Y. K. Xiang, , and T. Ha. Probing cellular protein complexes using single-molecule pull-down. *Nature*, 473:484–488, 2011.
- [28] D. Duzdevich and E. C. Greene. Towards physiological complexity with in vitro single-molecule biophysics. *Philosophical Transactions of the Royal Society B: Biological Sciences*, 368(1611), 2013.
- [29] P. F. Barbara, A. J. Gesquiere, S. Park, and Y. J. Lee. Single-molecule spectroscopy of conjugated polymers. *Accounts of Chemical Research*, 38(7):602–610, 2005.
- [30] X. Guo. Single-molecule electrical biosensors based on single-walled carbon nanotubes. *Advanced Materials*, 25:3397–3408, 2013.
- [31] B. N. G. Giepmans, S. R. Adams, M. H. Ellisman, and R. Y. Tsien. The fluorescent toolbox for assessing protein location and function. *Science*, 312:217–224, 2006.
- [32] S. R. Leslie, A. P. Fields, and A. E. Cohen. Convex lens-induced confinement for imaging single molecules. *Anal. Chem.*, 82:6224–6229, 2010.
- [33] J. Gorman and E. C. Greene. Visualizing one-dimensional diffusion of proteins along DNA. *Nature Structural & Molecular Biology*, 15(8):768–774, 2008.
- [34] B. Gibb, T. D. Silverstein, I. J. Finkelstein, and E. C. Greene. Single-stranded dna curtains for real-time single-molecule visualization of protein-nucleic acid interactions. *Analytical Chemistry*, 84(18):7607–7612, 2012.

- [35] Tim Sanchez, Daniel T N Chen, Stephen J DeCamp, Michael Heymann, and Zvonimir Dogic. Spontaneous motion in hierarchically assembled active matter. *Nature*, 491(7424):431–4, 2012.
- [36] M. W Elting and S. R. Leslie. Single-molecule fluorescence imaging of processive myosin with enhanced background suppression using linear zero-mode waveguides (ZMWs) and convex. *Optics Express*, 21(1):1189–1202, 2013.
- [37] D. J. Berard, F. Michaud, S. Mahshid, M. J. Ahamed, C. M. J. McFaul, J. S. Leith, P. Brub, R. Sladek, W. Reisner, and S. R. Leslie. Convex lens-induced nanoscale templating. *PNAS*, 111:1329513300, 2014.
- [38] C.E. Cordeiro, M. Molisana, and D. Thirumalai. Shape of confined polymer chains. *J. Phys. II France*, 7(3):433–447, 1997.
- [39] J. Tang, Stephen L. Levy, Daniel W. Trahan, Jeremy J. Jones, Harold G. Craighead, and Patrick S. Doyle. Revisiting the conformation and dynamics of dna in slitlike confinement. *Macromolecules*, 43:7368–7377, 2010.
- [40] J. Hohlbein, T. D. Craggs, and Thorben Cordes. Alternating-laser excitation: Single-molecule fret and beyond. *Chem. Soc. Rev.*, 43:1156, 2014.
- [41] D. M. Jameson and J. A. Ross. Fluorescence polarization/anisotropy in diagnostics and imaging. *Chem. Rev.*, 110:2685–2708, 2010.
- [42] G. D. Hamblin, A. A. Hariri, K. M. M. Carneiro, G. Cosa K. L. Lau, and H. F. Sleiman. Simple design for dna nanotubes from a minimal set of unmodified strands: Rapid, room-temperature assembly and readily tunable structure. *ACS Nano*, 7:30223028, 2013.
- [43] P.G. Wu and L Brand. Resonance energy transfer: Methods and applications. *Anal. Biochem.*, 218:1–13, 1994.
- [44] G. M. Whitesides and B Grzybowski. Self-assembly at all scales. *Science*, 295(5564):2418–21, 2002.